

Unsupervised Learning of Depth and Depth-of-Field Effect from Natural Images with Aperture Rendering Generative Adversarial Networks

Takuhiro Kaneko

NTT Communication Science Laboratories, NTT Corporation

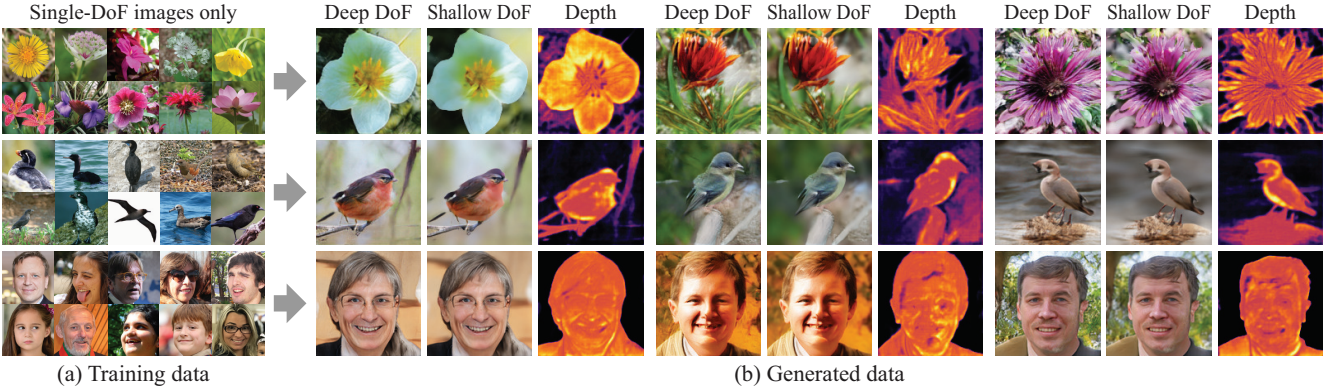


Figure 1. **Unsupervised learning of depth and depth-of-field (DoF) effect from unlabeled natural images.** (a) In training, we adopt only a collection of single-DoF images *without* any additional supervision (e.g., ground-truth depth, pairs of deep and shallow DoF images, and pretrained model). (b) Once trained, our model can synthesize tuples of deep and shallow DoF images and depths from random noise. The generated data are beneficial in training a shallow DoF renderer, which also requires *no* external supervision. The project page is available at <https://www.kecl.ntt.co.jp/people/kaneko.takuhiro/projects/ar-gan/>.

Abstract

Understanding the 3D world from 2D projected natural images is a fundamental challenge in computer vision and graphics. Recently, an unsupervised learning approach has garnered considerable attention owing to its advantages in data collection. However, to mitigate training limitations, typical methods need to impose assumptions for viewpoint distribution (e.g., a dataset containing various viewpoint images) or object shape (e.g., symmetric objects). These assumptions often restrict applications; for instance, the application to non-rigid objects or images captured from similar viewpoints (e.g., flower or bird images) remains a challenge. To complement these approaches, we propose aperture rendering generative adversarial networks (AR-GANs), which equip aperture rendering on top of GANs, and adopt focus cues to learn the depth and depth-of-field (DoF) effect of unlabeled natural images. To address the ambiguities triggered by unsupervised setting (i.e., ambiguities between smooth texture and out-of-focus blurs, and between foreground and background blurs), we develop DoF mixture learning, which enables the generator to learn real image distribution while generating diverse DoF images. In addition, we devise a center focus prior to guiding the learning direction. In the experiments, we demonstrate the effectiveness of AR-GANs in various datasets, such as flower, bird, and face images, demonstrate their portability by incorporating them into other 3D representation learning GANs, and validate their applicability in shallow DoF rendering.

1. Introduction

Natural images are 2D projections of a 3D world. Addressing the inverse problem, i.e., understanding the 3D world from natural images, is a fundamental challenge in computer vision and graphics. Owing to its diverse applications in various fields, such as in robotics, content creation, and photo editing, this challenge has been actively studied.

A direct solution to challenge is learning a 3D predictor in a supervised manner using 2D and 3D data pairs or multiview image sets. However, obtaining such data is often impractical or time-consuming. To eliminate this process, several studies have attempted to learn 3D representations from single-view images (i.e., with only a single view per training instance). However, owing to the ill-posed nature, several studies required auxiliary information, such as 2D keypoints [56, 25] or 2D silhouettes [18, 6, 36, 14], to align object positions or extract a target object from the background. Other studies required predefined category-specific shape models (e.g., 3DMM [3] and SMPL [40]) [24, 63, 12, 50, 51] to obtain clues for reconstruction. Although they have exhibited promising results, collecting auxiliary information still requires a laborious annotation process, and a shape model requires additional preparation costs and restricts applicable objects.

To eliminate these disadvantages, fully unsupervised learning methods that enable 3D representation learning from single-view images *without* additional supervision and shape models have been devised. Although this is a se-

vere setting, previous studies have addressed this challenge by imposing assumptions for viewpoint distribution (e.g., a dataset including various viewpoint images) [44, 54, 46] or object shape (e.g., symmetric objects) [67]. The first assumption is required to learn 3D representations by sampling diverse viewpoint images. The second assumption is required to perform stereo reconstruction using a pair of mirrored images. Although these assumptions are practical for objects of a specific class (e.g., human faces), several objects do not satisfy these assumptions. For example, these methods are difficult to apply to non-rigid objects or images captured from similar viewpoints (e.g., flower or bird images).

To broaden the application without contradicting previous achievements, in this study, we consider complementary cues inherent in photos that have not been actively used in previous deep generative models (including those above). In particular, we focus on *focus cues*, in other words, we consider the learning depth¹ and the depth-of-field (DoF) effect in the defocus process. Specifically, instead of imposing an assumption on the *viewpoint distribution*, we do so on the *DoF distribution* (i.e., a dataset including various DoF images), and as shown in Figure 1, we attempt to learn 3D representations (particularly *depth* and *DoF effect*) from a collection of single-DoF images (i.e., images with solely a single DoF setting per training instance).

To achieve this, we propose a novel family of generative adversarial networks (GANs) [15], referred to as *aperture rendering GANs* (AR-GANs), which equip aperture rendering (e.g., light field aperture rendering [53]) on top of GANs. Specifically, AR-GAN initially generates a pair of a deep DoF image and depth from a random noise, and then renders a shallow DoF image from the generated deep DoF image and depth via aperture rendering. With this mechanism, we can synthesize various DoF images using a virtual camera with an optical constraint on the light field.

When AR-GAN is trained in an unsupervised manner using single-DoF images, two non-trivial challenges are ambiguity between the smooth texture and out-of-focus blurs and ambiguity between the foreground and background blurs, as we cannot obtain explicit supervision of these relationships. For the first problem, we introduce *DoF mixture learning*, which enables the generator to learn the real image distribution while generating various DoF images. This learning ensures that the generated images (deep and shallow DoF images) are in real image distribution, and facilitates the learning of the depth, which is a source of connecting deep and shallow DoF images. For the second problem, based on the observed tendency to focus on the center object when a focused image is considered, we impose a *center focus prior*, which facilitates the focusing of the center while guiding the surroundings to be behind the focal plane. In practice, we adopt this prior solely at the beginning of training to guide the learning direction.

¹In this study, we use depth and disparity interchangeably to indicate disparity across a camera aperture.

To evaluate the effectiveness of AR-GAN, we first conducted experiments with comparative and ablation studies on diverse datasets, including flower (Oxford Flowers [45]), bird (CUB-200-2011 [60]), and face (FFHQ [29]) datasets. A significant property of AR-GAN is its portability, which we validated by incorporating AR-GAN into other 3D representation learning GANs (particularly, HoloGAN [44] and RGBD-GAN [46]). Another significant property of AR-GAN is its ability to synthesize a tuple of deep and shallow DoF images and depth from a random noise, after training. We utilize this property to train a shallow DoF renderer and empirically demonstrate its utility.

Overall, our contributions are summarized as follows:

- We provide *unsupervised learning of depth and DoF effect from unlabeled natural images*. This is noteworthy because it does not impose assumptions on the viewpoint distribution or object shape, which are required in conventional unsupervised 3D representation learning.
- To achieve this, we propose a novel GAN family (AR-GANs), which generate a deep DoF image and depth from a random noise and render a shallow DoF image from them via aperture rendering.
- To address ambiguities caused by a fully unsupervised setting, we devise *DoF mixture learning* to enable the generator to learn real image distribution using generated diverse DoF images, and develop a *center focus prior* to determine the learning direction.
- We validate the *effectiveness*, *portability*, and *applicability* of AR-GANs via extensive experiments. The project page is available at <https://www.kecl.ntt.co.jp/people/kaneko.takuhiro/projects/ar-gan/>.

2. Related work

Generative adversarial networks. GANs [15] have achieved remarkable success in 2D image modeling via a series of advancements (e.g., [5, 29, 30]). A substantial property of GANs is their ability to mimic data distribution in a random sampling process without explicitly defining the data distribution. This allows GANs to learn various distribution types. For example, recent studies [64, 66, 44, 18, 54, 46, 37] have made it possible to learn a 3D-aware image distribution via 3D GAN architectures or 3D representations. Among them, HoloGAN [44] and RGBD-GAN [46] share a similar motivation with us in terms of learning 3D representations from natural images in a fully unsupervised manner; however, the major difference is that they adopt *viewpoint cues*, whereas we employ *focus cues*. We empirically demonstrate this difference in Section 5.2. Owing to this difference, the previous and present models are not exchangeable but complementary. We verify their compatibility in Section 5.4 by combining AR-GAN with HoloGAN and RGBD-GAN.

Another related topic is the application of GANs for un-

supervised learning of the foreground and background [58, 71]. Although previous and present studies are relevant in terms of learning image compositions, they decompose the image *discretely*, whereas we learn the *continuous depth*. Furthermore, we can learn the *DoF effect*, which has not been achieved in previous studies.

Other relevant GANs are GANs with measurements [4, 47, 35, 26, 27], which apply measurements (e.g., mask and noise) before matching a generated image with a real image. Our aperture rendering functions similarly to those measurements. However, in the previous work, applicable measurements were limited to those in a *2D image plane*, and effectiveness was solely demonstrated on *synthetically corrupted* images. By contrast, AR-GAN can learn a DoF effect, which yields a *3D space*. In the experiments (Section 5), we verify that this effect can be learned from images taken in *real* scenarios.

Unsupervised 3D representation learning. As mentioned in Section 1, the learning of 3D representations from single-view images has garnered attention owing to its data collection advantage. To address this challenge, several studies have employed auxiliary information as clues for reconstruction, such as 2D keypoints [56, 25], 2D silhouettes [18, 6, 36, 14], or shape models [24, 63, 12, 50, 51]. By contrast, we attempt to address this challenge with *no* additional supervision and *no* predefined model to reduce costs from laborious annotation and model preparation.

Recently, some studies [44, 54, 46, 67] have addressed this; however, their assumptions and objectives differ from ours. They impose assumptions for the *viewpoint distribution* or *object shape*, whereas we impose an assumption for the *DoF distribution*. Owing to this assumption difference, they can learn *3D meshes* [54], *depth* [46, 67], *albedo* [67], *texture* [54], *light* [67], and *viewpoints* [44, 54, 46, 67], whereas AR-GAN can learn the *depth* and *DoF effect*. Therefore, AR-GAN can be considered a model that can complement (not replace) previous models. We validate this statement in Section 5.4 by incorporating AR-GAN into HoloGAN [44] and RGBD-GAN [46].

Monocular depth estimation. Monocular depth estimation involves predicting the depth when a single image is given. A successful approach involves training a depth predictor using paired or consecutive data, such as image and depth pairs [9, 38, 33, 32, 70, 10], stereo pairs [11, 13, 68], and videos [75, 72, 61]. Although this approach is a promising solution, collecting such data is often impractical or time-consuming.

In another direction, some studies [53, 16] have proposed the adoption of focused and all-in-focus image pairs, including learning the depth in the process of reconstructing the focused image from an all-in-focus image. Although this study is inspired by their success, the main difference is that they require paired supervision between focused and all-in-focus images, whereas ours does not need it. However, owing to this difference, our task is very challenging; therefore, in this study, we did not attempt to achieve high-

quality depth estimation comparable to supervised methods. Instead, in the experiments, we compared AR-GAN with a previous fully unsupervised depth estimation model (i.e., RGBD-GAN [46]) and demonstrated the utility of AR-GAN in this challenging setting (Section 5.2).

DoF rendering. The DoF or Bokeh effect is a popular photography technique, and its synthesis has garnered considerable interest in computer vision and graphics. To achieve this without prior knowledge of geometry and lightning, previous studies adopted stereo pairs [1], a stack of images taken in different camera settings [22, 17], and a segmentation mask [52, 59] to determine the degree of blur. Although they have exhibited remarkable results, they are limited owing to their general dependence on a manually defined DoF renderer. To address this limitation, end-to-end supervised learning methods [53, 62, 21, 48], which train a DoF renderer using pairs of shallow and deep DoF images, were devised. Recently, an unpaired learning method [76] was also proposed. This method eliminates the requirement for paired supervision; however, set-level supervision (i.e., supervision of whether each image is a deep or shallow DoF image) remains necessary. By contrast, we focus on training a DoF renderer in a *fully* unsupervised manner. We demonstrate the effectiveness of our approach in Section 5.5.

3. Preliminaries

3.1. GANs

We briefly introduce two previous works on which our model is based. The first is GAN [15], which learns data distribution using the following objective:

$$\mathcal{L}_{\text{GAN}} = \mathbb{E}_{I^r \sim p^r(I)} [\log C(I^r)] + \mathbb{E}_{z \sim p(z)} [\log(1 - C(G(z)))], \quad (1)$$

where, given a random noise z , a generator G generates an image $I^g = G(z)$ that can deceive a discriminator C by minimizing this objective, whereas C distinguishes I^g from a real image I^r by maximizing this objective. Here, superscripts r and g denote the real and generated data, respectively. Using this min-max game, the generative distribution $p^g(I)$ approaches the real distribution $p^r(I)$.

3.2. Light field aperture rendering

Light field aperture rendering [53] is a type of differentiable aperture rendering.² Its objective is to learn an aperture renderer R that synthesizes a shallow DoF image $I_s(\mathbf{x}) = R(I_d(\mathbf{x}), D(\mathbf{x}))$, given a deep DoF image $I_d(\mathbf{x})$ and depth $D(\mathbf{x})$.³ Here, \mathbf{x} represents the spatial coordinates

²Another representative aperture rendering is compositional aperture rendering [53], which discretely models disparities using a stack of blur kernels. In the initial experiments, we determined that light field aperture rendering, which models the light field within a camera, is more compatible with our unsupervised learning. This is possibly because the learning clues are few in our unsupervised learning; therefore, an explicit camera constraint via light field aperture rendering works sufficiently.

³In the original study [53], $D(\mathbf{x})$ is estimated from $I(\mathbf{x})$. However, this estimation is not adopted in AR-GAN; hence, we omitted it here.

of the light field on the image plane. When $I_d(\mathbf{x})$ is directly warped into the viewpoint in the light field based on $D(\mathbf{x})$, holes can appear in the resulting light field. Instead, a trainable neural network T is adopted to expand $D(\mathbf{x})$ into a depth map $M(\mathbf{x}, \mathbf{u})$ for each view in the light field:

$$M(\mathbf{x}, \mathbf{u}) = T(D(\mathbf{x})), \quad (2)$$

where \mathbf{u} denotes the angular coordinates of the light field on the aperture plane. Subsequently, $I_d(\mathbf{x})$ is warped into each view in the light field using the depth map $M(\mathbf{x}, \mathbf{u})$:⁴

$$L(\mathbf{x}, \mathbf{u}) = I_d(\mathbf{x} + \mathbf{u}M(\mathbf{x}, \mathbf{u})), \quad (3)$$

where $L(\mathbf{x}, \mathbf{u})$ is the simulated camera light field. Finally, it is integrated to render a shallow DoF image $I_s(\mathbf{x})$:

$$I_s(\mathbf{x}) = \sum_{\mathbf{u}} A(\mathbf{u})L(\mathbf{x}, \mathbf{u}), \quad (4)$$

where $A(\mathbf{u})$ is an indicator that represents the disk-shaped camera aperture. Hereafter, for simplicity, we omit \mathbf{x} and \mathbf{u} when they are not required.

4. Aperture rendering GANs: AR-GANs

4.1. Problem statement

We begin by defining the problem statement. We consider a fully unsupervised setting in which we cannot obtain any supervision or pretrained model except for an image collection. As discussed in Section 2, typical end-to-end focus-based monocular depth estimation methods (e.g., [53, 16]), and DoF rendering methods (e.g., [53, 21, 48, 76]) achieve their objectives using a *conditional* model (i.e., a deep DoF image is used as the input, and a depth or shallow DoF image is estimated based on it). However, in our fully unsupervised setting, we cannot employ this formulation as we cannot obtain either ground-truth depth or supervision of whether each image is a deep or shallow DoF image.

Alternatively, we aim to learn an *unconditional* generator $G(z)$ that can generate a tuple of a deep DoF image, depth, and shallow DoF image, i.e., (I_d^g, D^g, I_s^g) , from a random noise z . When the training images are extremely biased in terms of the DoF (e.g., all images are all-in-focus), it is difficult to obtain focus cues from the images; hence, we impose the following assumption on an image distribution:

Assumption 1 *The DoF setting is different for each image, and the dataset includes various DoF images.*

Note that we do not have to collect a *set/pair* of various DoF images for each training instance. We observed that this assumption is satisfied by typical natural image datasets (e.g., flower [45], bird [60], and face [29] datasets shown in Figure 1). Under this assumption, we aim to learn the above-mentioned generator in a *wisdom of crowds* approach.

⁴The depth of the focal plane can be learned explicitly by adding the parameterized offset \hat{m} to M in Equation 3. However, we do not do so under the assumption that it is determined per image I_d and internally represented and optimized in D , which is used in Equation 2. In this case, the focal plane exists at $D = 0$, while out-of-focus occurs in $|D| > 0$.

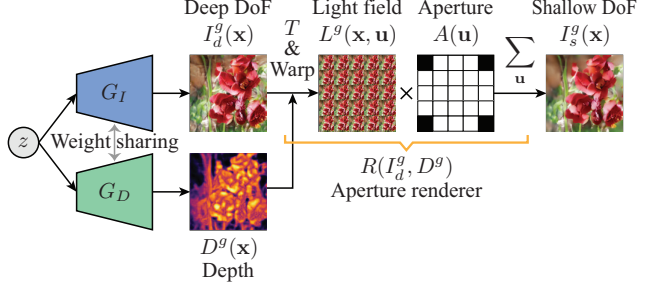


Figure 2. **Overall pipeline of AR-GAN generator.** The AR-GAN generator first generates a deep DoF image I_d^g and depth D^g from a random noise z , and then renders a shallow DoF image I_s^g from I_d^g and D^g using the aperture renderer R .

4.2. Overall pipeline

The overall pipeline of the AR-GAN generator is illustrated in Figure 2. When given a random noise z , we first generate a deep DoF image I_d^g and depth D^g as follows:

$$I_d^g = G_I(z), D^g = G_D(z). \quad (5)$$

In practice, we share the weights between G_I and G_D except for the last layer because the image and depth exhibit high correlation. A previous study [39] demonstrated that this kind of weight sharing is beneficial in learning a joint distribution between relevant domains. Subsequently, we render a shallow DoF image I_s^g from the generated I_d^g and D^g using the aperture renderer R described in Section 3.2.

Typical GANs apply a discriminator C to the final output of the generator (i.e., I_s^g in our case). However, in AR-GAN, both generators (i.e., G_I and G_D) and R are trainable. Hence, without constraints, they could compete for roles. For example, they can drift into an extreme solution (e.g., R learns strong out-of-focus, and G_I learns an over-deblurred image). To address this, we develop *DoF mixture learning*, which is detailed in the next section.

4.3. DoF mixture learning

A possible solution to this problem is regularizing G_I using an explicit distance metric (e.g., L1, L2, or perceptual loss [23, 8]) such that I_d^g is approximate to I_s^g . However, this solution disrupts the depth learning (Section 5.3.1).

Alternatively, we introduce *DoF mixture learning*. Figure 3 illustrates the comparison between standard and DoF mixture learning. In standard GAN training, the generator attempts to cover the real image distribution using images without constraints. By contrast, in the DoF mixture learning, the generator attempts to represent the real image distribution using diverse DoF images whose extent is adjusted by a scale factor s . More precisely, in our AR-GAN, the GAN objective (Equation 1) is rewritten as follows:

$$\begin{aligned} \mathcal{L}_{\text{AR-GAN}} = & \mathbb{E}_{I^r \sim p^r(I)} [\log C(I^r)] \\ & + \mathbb{E}_{z \sim p(z), s \sim p(s)} [\log(1 - C(R(G_I(z), sG_D(z))))], \end{aligned} \quad (6)$$

where $s \in [0, 1]$; when $s = 0$, a deep DoF image (almost equal to I_d^g) is rendered, whereas when $s = 1$, a shallow

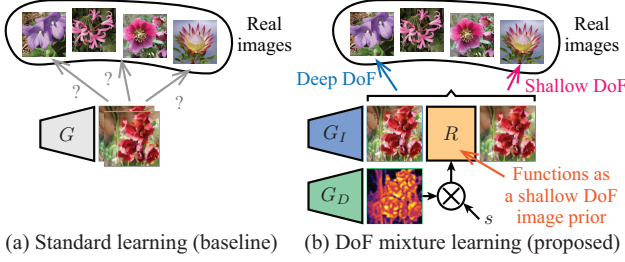


Figure 3. **Comparison of standard and DoF mixture learning.**

DoF image (I_s^g) is rendered. Intuitively, the aperture renderer R , which has an optical constraint on the light field, functions as a shallow DoF image prior. Under Assumption 1 (a real image distribution $p^r(I)$ includes both deep I_d^r and shallow I_s^r DoF images), this prior encourages the generated deep I_d^g and shallow I_s^g DoF images to approximate I_d^r and I_s^r , respectively. This also facilitates the learning of D^g , which is a source of the I_d^g and I_s^g connection.

In practice, we determined that sampling s from a binomial distribution, i.e., $p(s) = B(1, p_s)$, works optimally, where p_s indicates a probability of $s = 1$. In Section 5.3, we examine the effect of the p_s value. It was manually determined for simplicity; however, optimizing it in a data-driven approach is a potential direction for future work.

4.4. Center focus prior

Another challenge unique to unsupervised depth and DoF effect learning is to the difficulty in distinguishing foreground and background blurs without any constraint or prior knowledge. Although not all images satisfy this, focused images tend to be captured when the main targets are positioned at the center, as shown in Figure 4(a). Based on this observation, we impose a center focus prior defined by

$$D_p = \begin{cases} 0 & (r \leq r_{th}) \\ -g \cdot (r - r_{th}) & (r > r_{th}), \end{cases} \quad (7)$$

where r indicates the distance from the center of the image, and r_{th} and g denote the hyper-parameters that define the focused area and depth gain, respectively. We visualize this prior in Figure 4(b). As shown in this figure, the prior facilitates the center area focus while promoting the surrounding area to be behind the focal plane. We apply this prior to the generated depth D^g as follows:

$$\mathcal{L}_p = \lambda_p \|D^g - D_p\|_2^2, \quad (8)$$

where λ_p represents a weighting parameter. In practice, we apply this only at the beginning of training to mitigate the negative effect triggered by the gap between D^r and D_p .



Figure 4. **Examples of focused images and center focus prior.** In (b), light color indicates the foreground.

5. Experiments

5.1. Experimental settings

We conducted four experiments to verify the effectiveness of AR-GANs from multiple perspectives: a comparative study on unsupervised 3D representation learning (Section 5.2), ablation studies on DoF mixture learning and center focus prior (Section 5.3), portability analysis (Section 5.4), and application in shallow DoF rendering (Section 5.5). Here, we explain the common settings and present the details of each in the following sections.

Datasets. We evaluated AR-GANs on three natural image datasets that cover various objects: Oxford Flowers [45] (8189 flower images with 102 categories), CUB-200-2011 [60] (11788 bird images with 200 categories), and FFHQ [29] (70000 face images). To efficiently examine various cases, we resized the images to 64×64 . We also experimented on 128×128 images in some cases to confirm the dependency on image resolution (e.g., Figure 1).

Metrics. To evaluate the visual fidelity of the generated images, we adopted the *kernel inception distance* (KID) [2],⁵ which computes the maximum mean discrepancy between real and generated images within the Inception model [55]. When calculating scores, we generated 20000 images from each model. Measuring depth and DoF accuracy directly is non-trivial because we aim to learn an unconditional model from unpaired and unlabeled natural images, and cannot obtain the ground truth. Alternatively, we evaluated the depth accuracy by (1) learning the depth estimator using pairs of images and depths generated by GANs, (2) predicting the depths of real images using the learned depth estimator, and (3) comparing the obtained results with the depths predicted by a state-of-the-art monocular depth estimator [68], which is trained using stereo pairs in an external dataset.⁶ We used *scale-invariant depth error* (SIDE) [9] to measure the difference. In both metrics, the performance increased as the score decreased. In all the experiments, we report the mean score with the standard deviation over three training runs.

Implementation. We implemented the model based on HoloGAN [44]. The generator has a StyleGAN-like architecture [29]. In AR-GANs, 3D convolution used in HoloGAN is not required; hence, we replaced it with 2D convolution. The discriminator has instance [57] and spectral [42] normalizations. The networks were trained using the Adam optimizer [31] with a non-saturating GAN loss [15].

5.2. Comparative study

First, we conducted a comparative study to clarify the difference between AR-GAN and previous fully unsupervised 3D representation learning.

⁵We used KID because it has an unbiased estimator and complements the flaws of other representative metrics (i.e., Fréchet inception distance (FID) [19] and inception score (IS) [19]).

⁶We used the pretrained model provided by the authors: <https://github.com/KexianHust/Structure-Guided-Ranking-Loss>.

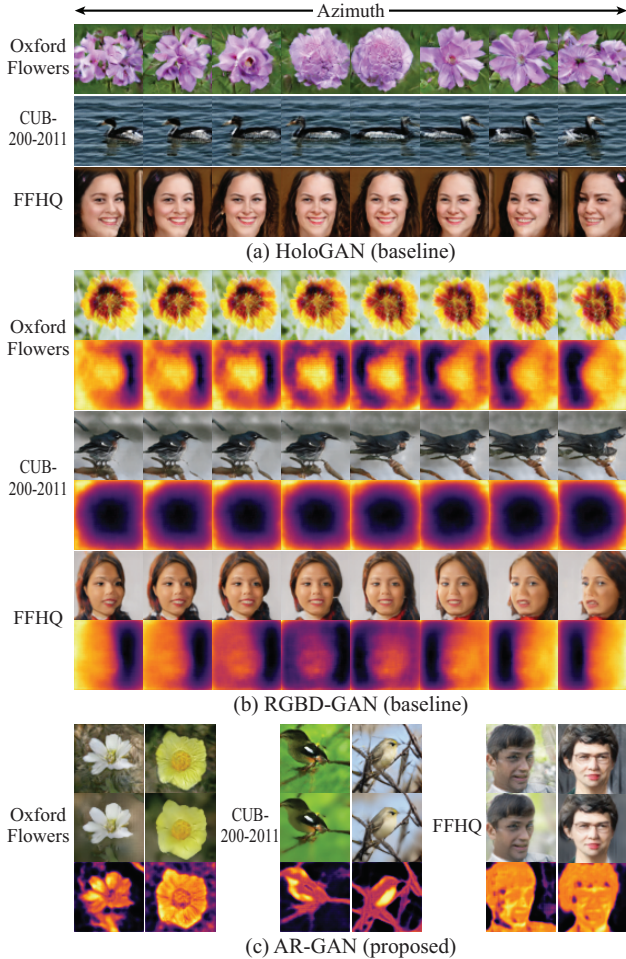


Figure 5. **Qualitative comparison among HoloGAN, RGBD-GAN, and AR-GAN.** HoloGAN, RGBD-GAN, and AR-GAN generate images, image and depth pairs, and tuples of deep and shallow DoF images and depths, respectively.

Comparison models. We compared AR-GAN with *HoloGAN* [44] and *RGBD-GAN* [46], which are representative models in this category, as well as standard GAN [15]. As discussed in Section 2, HoloGAN/RGBD-GAN learns 3D representations using *viewpoint cues*, whereas AR-GAN achieves this with *focus cues*. Hence, the applicable datasets are different, which we verified by using the three datasets.

Results. Examples of the generated images are presented in Figure 5. Here, the obtainable 3D representations and applicable datasets differ among the GANs. Although HoloGAN and RGBD-GAN succeed in learning viewpoint-aware representations in FFHQ, they fail to do so in Oxford Flowers and CUB-200-2011, where viewpoint distributions are biased and viewpoint cues do not exist sufficiently. By contrast, AR-GAN succeeds in learning the depth and DoF effect in all datasets because it can employ focus cues, which are present across all datasets.

The KID comparison is summarized in Table 1. We found that AR-GAN achieved comparable performance and did not incur a negative effect across all datasets.

$KID \times 10^3 \downarrow$	Oxford Flowers	CUB-200-2011	FFHQ
GAN	11.71 ± 0.68	15.04 ± 0.14	6.97 ± 0.30
HoloGAN	11.30 ± 0.37	14.68 ± 0.51	6.89 ± 0.38
RGBD-GAN	12.04 ± 0.35	14.92 ± 0.49	6.73 ± 0.26
AR-GAN	11.23 ± 0.36	14.30 ± 0.56	5.75 ± 0.19

Table 1. **Comparison of $KID \times 10^3 \downarrow$ among different GANs.**

$SIDE \times 10^2 \downarrow$	Oxford Flowers	CUB-200-2011	FFHQ
RGBD-GAN	7.01 ± 0.81	7.06 ± 0.02	5.81 ± 0.40
AR-GAN	4.46 ± 0.03	3.58 ± 0.04	4.21 ± 0.15

Table 2. **Comparison of $SIDE \times 10^2 \downarrow$ between RGBD-GAN and AR-GAN.** GAN and HoloGAN are not listed here because they cannot generate depth along with an image.

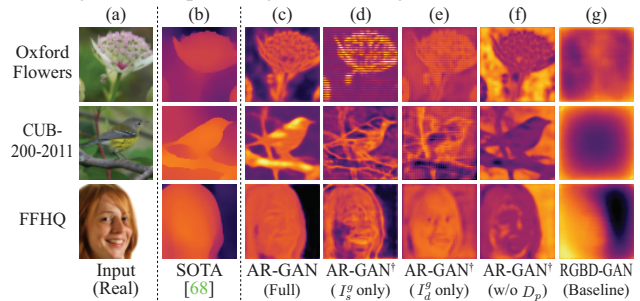


Figure 6. **Examples of predicted depths.** \dagger indicates the ablated model. (c–g) Results obtained in a fully unsupervised setting.

The SIDE comparison is presented in Table 2. We found that AR-GAN outperforms RGBD-GAN in all datasets. Examples of the predicted depths are presented in Figure 6. Although the predicted depths exhibit a lower resolution than those predicted by the supervised methods (e.g., [68]),⁷ we found that AR-GAN (c) improves the details (e.g., flower details and tree branches) that disappear in [68] (b) and RGBD-GAN (g), thus benefiting from focus cues.

5.3. Ablation study

5.3.1 Ablation study on DoF mixture learning

Metrics. We first evaluated the importance of the DoF mixture learning. As mentioned in Section 5.1, measuring depth and DoF accuracy directly is non-trivial; therefore, we further adopted two metrics along with KID and SIDE: (1) *Learned perceptual image patch similarity (LPIPS)* [73] computes the distance between two images in the CNN feature space and is demonstrated to exhibit a high correlation with human perceptual similarity [73]. We adopted LPIPS to measure the perceptual similarity between pairs of I_d^g and I_s^g . LPIPS is expected to be moderately small because the content is preserved before and after the application of aperture rendering. (2) *Depth standard deviation (DSD)* is the standard deviation of the generated depths. Our objective is to learn a meaningful depth that can yield a plausible DoF effect. When depth learning is successful, DSD is expected to be sufficiently large.

⁷Note that 64×64 is the standard resolution for fully unsupervised learning methods (e.g., HoloGAN and RGBD-GAN), and applications to images with complex objects/backgrounds are challenging for them.

Oxford Flowers	KID $\times 10^3\downarrow$	SIDE $\times 10^2\downarrow$	LPIPS \downarrow	DSD \uparrow
I_d^g only $p_s = 1$	12.36 ± 0.59	5.48 ± 0.20	0.229 ± 0.027	0.157 ± 0.063
Mixture $p_s = 0.75$	10.97 ± 0.26	4.81 ± 0.06	0.023 ± 0.001	0.657 ± 0.006
Mixture $p_s = 0.5$	10.69 ± 0.48	4.65 ± 0.05	0.022 ± 0.000	0.771 ± 0.022
Mixture $p_s = 0.25$	11.23 ± 0.36	4.46 ± 0.03	0.028 ± 0.001	1.007 ± 0.025
I_d^g only $p_s = 0$	11.58 ± 0.37	4.56 ± 0.20	0.113 ± 0.013	0.446 ± 0.065
L1	11.66 ± 0.72	5.26 ± 0.65	0.033 ± 0.001	0.387 ± 0.116
Double discriminators	9.74 ± 0.31	6.79 ± 2.21	0.000 ± 0.001	0.032 ± 0.046

CUB-200-2011	KID $\times 10^3\downarrow$	SIDE $\times 10^2\downarrow$	LPIPS \downarrow	DSD \uparrow
I_d^g only $p_s = 1$	13.62 ± 0.53	4.63 ± 0.50	0.125 ± 0.037	0.354 ± 0.021
Mixture $p_s = 0.75$	12.68 ± 0.61	3.75 ± 0.08	0.037 ± 0.003	0.748 ± 0.072
Mixture $p_s = 0.5$	13.14 ± 0.03	3.55 ± 0.02	0.043 ± 0.003	0.959 ± 0.075
Mixture $p_s = 0.25$	14.30 ± 0.56	3.58 ± 0.04	0.059 ± 0.002	1.175 ± 0.017
I_d^g only $p_s = 0$	14.58 ± 0.56	5.94 ± 0.70	0.115 ± 0.019	0.193 ± 0.012
L1	12.54 ± 0.32	5.75 ± 1.26	0.042 ± 0.001	0.725 ± 0.195
Double discriminators	12.50 ± 0.12	4.33 ± 0.34	0.000 ± 0.000	0.001 ± 0.000

FFHQ	KID $\times 10^3\downarrow$	SIDE $\times 10^2\downarrow$	LPIPS \downarrow	DSD \uparrow
I_d^g only $p_s = 1$	5.75 ± 0.44	6.00 ± 0.35	0.097 ± 0.011	0.296 ± 0.018
Mixture $p_s = 0.75$	5.67 ± 0.23	4.38 ± 0.10	0.009 ± 0.001	0.757 ± 0.177
Mixture $p_s = 0.5$	5.75 ± 0.19	4.21 ± 0.15	0.009 ± 0.001	0.769 ± 0.119
Mixture $p_s = 0.25$	6.17 ± 0.08	4.68 ± 0.33	0.010 ± 0.001	0.583 ± 0.071
I_d^g only $p_s = 0$	6.85 ± 0.13	4.77 ± 0.13	0.028 ± 0.006	0.202 ± 0.003
L1	5.82 ± 0.21	4.82 ± 0.09	0.015 ± 0.004	0.466 ± 0.045
Double discriminators	6.20 ± 0.08	5.20 ± 0.47	0.000 ± 0.000	0.000 ± 0.000

Table 3. Comparison of KID $\times 10^3\downarrow$, SIDE $\times 10^2\downarrow$, LPIPS \downarrow , and DSD \uparrow among AR-GANs with different learning methods.

Comparison models. We conducted the analysis from two perspectives. (1) We evaluated the effect of the p_s value, which indicates the rate of using shallow DoF images in the DoF mixture learning (Equation 6). (2) We tested two possible alternatives: *L1*, which uses L1 loss to guide I_d^g closer to I_s^g , and *double discriminators*, which adopts two discriminators, for I_d^g and I_s^g , respectively. This facilitates both $p^g(I_d)$ and $p^g(I_s)$ to coincide with the overall real distribution $p^r(I)$.

Results. A comparison of the scores is summarized in Table 3. Our main findings are two-fold:

(1) *Effect of value of p_s .* We found that some fluctuations exist in the KID; however, in all cases, the scores are comparable to those of the other GANs presented in Table 1. This indicates that AR-GANs can generate plausible images regardless of p_s . By contrast, SIDE, LPIPS, and DSD are affected by p_s . SIDE tends to improve when the DoF mixture learning is adopted.⁸ This is because in the DoF mixture learning, we can encourage I_d^g and I_s^g to approximate I_d^r and I_s^r , respectively, as well as facilitate D^g learning, which is the source that connects them. Examples of predicted depths (Figure 6 (c-e)) also validate the effectiveness of DoF mixture learning. Regarding LPIPS and DSD, as LPIPS increases, and DSD successively decreases when $p_s = 1$ or $p_s = 0$. This indicates that the DoF mixture learning is required to manage LPIPS and DSD. Among AR-GANs with DoF mixture learning (i.e., $p_s \in \{0.25, 0.5, 0.75\}$), there is a trade-off and dataset dependency relative to LPIPS and DSD. Consider the score

⁸The sole “ I_d^g only” case in Oxford Flowers is an exception. In this case, D^g is not regularized by aperture rendering; however, weight sharing between G_I and G_D (Section 4.2) aids the depth learning. This strategy exhibits dataset dependency and fails in the other datasets.

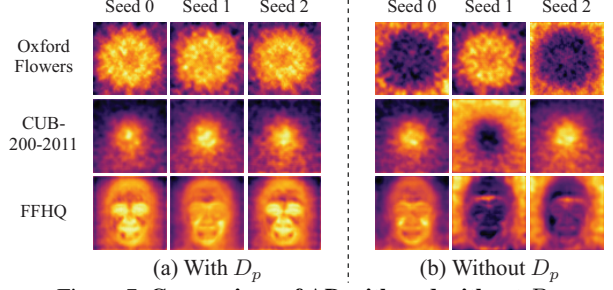


Figure 7. Comparison of AD with and without D_p .

Oxford Flowers	KID $\times 10^3\downarrow$	SIDE $\times 10^2\downarrow$	LPIPS \downarrow	DSD \uparrow
W/ D_p	11.23 ± 0.36	4.46 ± 0.03	0.028 ± 0.001	1.007 ± 0.025
W/o D_p	10.69 ± 0.24	6.78 ± 1.58	0.026 ± 0.002	0.915 ± 0.137

CUB-200-2011	KID $\times 10^3\downarrow$	SIDE $\times 10^2\downarrow$	LPIPS \downarrow	DSD \uparrow
W/ D_p	14.30 ± 0.56	3.58 ± 0.04	0.059 ± 0.002	1.175 ± 0.017
W/o D_p	13.96 ± 0.63	4.86 ± 1.84	0.062 ± 0.004	1.183 ± 0.059

FFHQ	KID $\times 10^3\downarrow$	SIDE $\times 10^2\downarrow$	LPIPS \downarrow	DSD \uparrow
W/ D_p	5.75 ± 0.19	4.21 ± 0.15	0.009 ± 0.001	0.769 ± 0.119
W/o D_p	5.72 ± 0.10	6.70 ± 1.88	0.009 ± 0.001	0.851 ± 0.057

Table 4. Comparison of KID $\times 10^3\downarrow$, SIDE $\times 10^2\downarrow$, LPIPS \downarrow , and DSD \uparrow among AR-GANs with and without D_p .

balance, we set $p_s = 0.25$ for Oxford Flowers and CUB-200-2011 and $p_s = 0.5$ for FFHQ in other experiments.

(2) *Comparison with alternatives.* Although L1 achieves reasonable LPIPS, it deteriorates SIDE and DSD more than those in the DoF mixture learning. This result indicates that this method disrupts depth learning. Double discriminators facilitate both $p^g(I_d)$ and $p^g(I_s)$ to coincide with $p^r(I)$. Consequently, LPIPS and DSD approach zero, and SIDE depreciates. This result verifies the importance of mixing I_d^g and I_s^g when learning $p^r(I)$.

5.3.2 Ablation study on center focus prior

Metrics. We evaluated the necessity of the center focus prior D_p . To assess the overall tendency of each pixel to represent the foreground or background blur, we calculated the *average depth (AD)*, i.e., the pixel-wise average of the generated depths. To validate the learning consistency, we compared the results over three training runs.

Results. The results are presented in Figure 7. We found that we can obtain constant results across training runs when D_p is adopted. In all results, the center is focused, while the surroundings are behind the focal plane. By contrast, when we eliminate D_p , the foreground and background are turned over, depending on the initialization. These results indicate that D_p is beneficial in determining the learning direction.

The comparison of the scores is summarized in Table 4. We found that KID, LPIPS, and DSD are comparable across all datasets. We deduce that D_p is solely adopted at the beginning of training; therefore, it does not disrupt the entire training. By contrast, SIDE depreciates when D_p is not implemented. This occurs because the foreground and background are reversed, as shown in Figure 6(f).

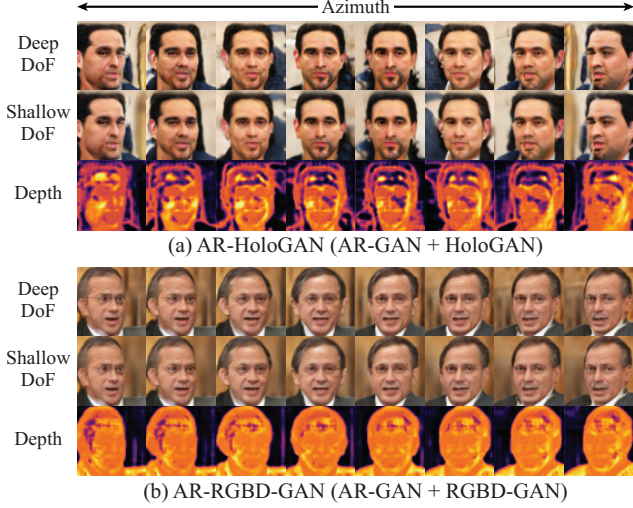


Figure 8. **Examples of data generated using AR-HoloGAN and AR-RGBD-GAN.** The viewpoint change in the horizontal direction is obtained by the HoloGAN/RGBD-GAN function, whereas the DoF change and depth in the vertical direction are obtained by the AR-GAN function.

5.4. Portability analysis

As presented in Section 5.2, the obtainable representations differ between HoloGAN/RGBD-GAN and AR-GAN. An interesting approach would be learning these representations jointly by combining them. A significant property of AR-GAN is *portability*, i.e., it is easy to incorporate into other GANs. Specifically, we can achieve this simply by adding aperture rendering on top of HoloGAN/RGBD-GAN and training it with the DoF mixture training and a center focus prior. One requirement is that a dataset should satisfy the assumptions of both models; i.e., a dataset should include diverse viewpoint images along with various DoF images. Among the datasets described above, only FFHQ satisfies this requirement. Hence, we solely evaluated *AR-HoloGAN* (AR-GAN + HoloGAN) and *AR-RGBD-GAN* (AR-GAN + RGBD-GAN) on this dataset.

Results. Examples of generated data are shown in Figure 8. As shown in this figure, we can jointly control both viewpoints and the DoF effect with the HoloGAN/RGBD-GAN and AR-GAN functions. As a reference, we also calculated the KID scores. The scores for AR-HoloGAN and AR-RGBD-GAN were 5.70 ± 0.32 and 5.43 ± 0.22 , respectively. These are better than the scores of the original AR-GAN, HoloGAN, and RGBD-GAN (Table 1).

5.5. Application in shallow DoF rendering

Finally, we demonstrate the applicability of AR-GAN in shallow DoF rendering. After training, AR-GAN can synthesize tuples of (I_d^g, D^g, I_s^g) from random noise. By utilizing this, we learn a shallow DoF renderer $I_d \rightarrow I_s$ using pairs of (I_d^g, I_s^g) . We call this approach *AR-GAN-R*. As another approach, we learn a depth estimator $I_d \rightarrow D$ using pairs of (I_d^g, D^g) . By employing the learned depth estimator,

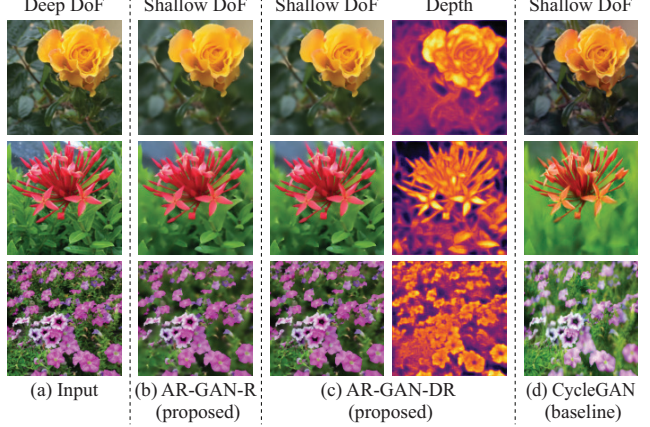


Figure 9. **Examples of shallow DoF rendering.**

tor, we estimate D from I_d and then render I_s from (I_d, D) using R in AR-GAN. We call this approach *AR-GAN-DR*.

Dataset. We used Oxford Flowers and AR-GAN-generated images to train AR-GAN and AR-GAN-R/DR, respectively. To confirm generality, we conducted a test on a different dataset, including flower photos taken by smartphones, which were used in the CycleGAN study [76].

Comparison model. To the best of our knowledge, no previous method can learn the DoF effect from natural images in the same setting as ours (i.e., *without* additional supervision and a predefined model). Therefore, as a baseline, we used CycleGAN [76], which trains a shallow DoF renderer $I_d \rightarrow I_s$ using *set-level* supervision (i.e., supervision of whether each image is a deep or shallow DoF image).⁹

Results. Examples of the rendered images are presented in Figure 9. We found that CycleGAN often yields unnecessary changes (e.g., color change), whereas AR-GAN-R/DR does not. We infer that the aperture rendering mechanism in AR-GAN contributes to this phenomenon. In addition, AR-GAN-DR can estimate the depth simultaneously.

6. Conclusion

We proposed a novel family of GANs, AR-GANs, which can learn depth and DoF effect from unconstrained natural images. To achieve this, we incorporated aperture rendering into GANs and developed DoF mixture learning and a center focus prior to address the ambiguities triggered by the unsupervised setting. Via comparative and ablation studies, we elucidated the differences from previous GANs and the significance of the proposed techniques. We demonstrated that AR-GANs are compatible and complementary to previous GANs by combining AR-GANs with HoloGAN/RGBD-GAN. Finally, we demonstrated the applicability of AR-GANs in shallow DoF rendering. Despite their applications in photos, several deep generative models do not utilize focus cues. In the future, we expect that our findings will facilitate further studies on such models.

⁹We used the pretrained model provided by the authors: <https://github.com/junyanz/pytorch-CycleGAN-and-pix2pix>.

References

- [1] Jonathan T. Barron, Andrew Adams, YiChang Shih, and Carlos Hernández. Fast bilateral-space stereo for synthetic defocus. In *CVPR*, 2015. 3
- [2] Mikołaj Bińkowski, Dougal J Sutherland, Michael Arbel, and Arthur Gretton. Demystifying MMD GANs. In *ICLR*, 2018. 5, 11
- [3] Volker Blanz and Thomas Vetter. A morphable model for the synthesis of 3D faces. In *SIGGRAPH*, 1999. 1
- [4] Ashish Bora, Eric Price, and Alexandros G. Dimakis. AmbientGAN: Generative models from lossy measurements. In *ICLR*, 2018. 3
- [5] Andrew Brock, Jeff Donahue, and Karen Simonyan. Large scale GAN training for high fidelity natural image synthesis. In *ICLR*, 2019. 2
- [6] Wenzheng Chen, Huan Ling, Jun Gao, Edward Smith, Jaakko Lehtinen, Alec Jacobson, and Sanja Fidler. Learning to predict 3D objects with an interpolation-based differentiable renderer. In *NeurIPS*, 2019. 1, 3
- [7] Terrance DeVries and Graham W. Taylor. Improved regularization of convolutional neural networks with cutout. *arXiv preprint arXiv:1708.04552*, 2017. 24
- [8] Alexey Dosovitskiy and Thomas Brox. Generating images with perceptual similarity metrics based on deep networks. In *NIPS*, 2016. 4, 14
- [9] David Eigen, Christian Puhrsch, and Rob Fergus. Depth map prediction from a single image using a multi-scale deep network. In *NIPS*, 2014. 3, 5, 11
- [10] Huan Fu, Mingming Gong, Chaohui Wang, Kayhan Batmanghelich, and Dacheng Tao. Deep ordinal regression network for monocular depth estimation. In *CVPR*, 2018. 3
- [11] Ravi Garg, Vijay Kumar B G, Gustavo Carneiro, and Ian Reid. Unsupervised CNN for single view depth estimation: Geometry to the rescue. In *ECCV*, 2016. 3
- [12] Baris Gecer, Stylianos Ploumpis, Irene Kotsia, and Stefanos Zafeiriou. GANFIT: Generative adversarial network fitting for high fidelity 3D face reconstruction. In *CVPR*, 2019. 1, 3
- [13] Clément Godard, Oisín Mac Aodha, and Gabriel J. Brostow. Unsupervised monocular depth estimation with left-right consistency. In *CVPR*, 2017. 3
- [14] Shubham Goel, Angjoo Kanazawa, and Jitendra Malik. Shape and viewpoint without keypoints. In *ECCV*, 2020. 1, 3
- [15] Ian J. Goodfellow, Jean Pouget-Abadie, Mehdi Mirza, Bing Xu, David Warde-Farley, Sherjil Ozair, Aaron Courville, and Yoshua Bengio. Generative adversarial nets. In *NIPS*, 2014. 2, 3, 5, 6, 24
- [16] Shir Gur and Lior Wolf. Single image depth estimation trained via depth from defocus cues. In *CVPR*, 2019. 3, 4
- [17] Samuel W. Hasinoff and Kiriakos N. Kutulakos. A layer-based restoration framework for variable-aperture photography. In *ICCV*, 2007. 3
- [18] Philipp Henzler, Niloy Mitra, and Tobias Ritschel. Escaping Plato’s cave using adversarial training: 3D shape from unstructured 2D image collections. In *ICCV*, 2019. 1, 2, 3
- [19] Martin Heusel, Hubert Ramsauer, Thomas Unterthiner, Bernhard Nessler, Günter Klambauer, and Sepp Hochreiter. GANs trained by a two time-scale update rule converge to a Nash equilibrium. In *NIPS*, 2017. 5
- [20] Xun Huang and Serge Belongie. Arbitrary style transfer in real-time with adaptive instance normalization. In *ICCV*, 2017. 23
- [21] Andrey Ignatov, Jagruti Patel, and Radu Timofte. Rendering natural camera bokeh effect with deep learning. In *CVPR Workshop*, 2020. 3, 4
- [22] David E. Jacobs, Jongmin Baek, and Marc Levoy. Focal stack compositing for depth of field control. *Stanford Computer Graphics Laboratory Technical Report*, 1(1):2012, 2012. 3
- [23] Justin Johnson, Alexandre Alahi, and Li Fei-Fei. Perceptual losses for real-time style transfer and super-resolution. In *ECCV*, 2016. 4, 14
- [24] Angjoo Kanazawa, Michael J. Black, David W. Jacobs, and Jitendra Malik. End-to-end recovery of human shape and pose. In *CVPR*, 2018. 1, 3
- [25] Angjoo Kanazawa, Shubham Tulsiani, Alexei A. Efros, and Jitendra Malik. Learning category-specific mesh reconstruction from image collections. In *ECCV*, 2018. 1, 3
- [26] Takuhiro Kaneko and Tatsuya Harada. Noise robust generative adversarial networks. In *CVPR*, 2020. 3
- [27] Takuhiro Kaneko and Tatsuya Harada. Blur, noise, and compression robust generative adversarial networks. In *CVPR*, 2021. 3
- [28] Tero Karras, Timo Aila, Samuli Laine, and Jaakko Lehtinen. Progressive growing of GANs for improved quality, stability, and variation. In *ICLR*, 2017. 24
- [29] Tero Karras, Samuli Laine, and Timo Aila. A style-based generator architecture for generative adversarial networks. In *CVPR*, 2019. 2, 4, 5, 23
- [30] Tero Karras, Samuli Laine, Miika Aittala, Janne Hellsten, Jaakko Lehtinen, and Timo Aila. Analyzing and improving the image quality of StyleGAN. In *CVPR*, 2020. 2
- [31] Diederik P. Kingma and Jimmy Ba. Adam: A method for stochastic optimization. In *ICLR*, 2015. 5, 23, 24, 25
- [32] Yevhen Kuznetsov, Jorg Stuckler, and Bastian Leibe. Semi-supervised deep learning for monocular depth map prediction. In *CVPR*, 2017. 3
- [33] Iro Laina, Christian Rupprecht, Vasileios Belagiannis, Federico Tombari, and Nassir Navab. Deeper depth prediction with fully convolutional residual networks. In *3DV*, 2016. 3
- [34] Christian Ledig, Lucas Theis, Ferenc Huszar, Jose Caballero, Andrew Cunningham, Alejandro Acosta, Andrew Aitken, Alykhan Tejani, Johannes Totz, Zehan Wang, and Wenzhe Shi. Photo-realistic single image super-resolution using a generative adversarial network. In *CVPR*, 2017. 14
- [35] Steven Cheng-Xian Li, Bo Jiang, and Benjamin Marlin. MisGAN: Learning from incomplete data with generative adversarial networks. In *ICLR*, 2019. 3
- [36] Xueting Li, Sifei Liu, Kihwan Kim, Shalini De Mello, Varun Jampani, Ming-Hsuan Yang, and Jan Kautz. Self-supervised single-view 3D reconstruction via semantic consistency. In *ECCV*, 2020. 1, 3
- [37] Yiyi Liao, Katja Schwarz, Lars Mescheder, and Andreas Geiger. Towards unsupervised learning of generative models for 3D controllable image synthesis. In *CVPR*, 2020. 2
- [38] Fayao Liu, Chunhua Shen, Guosheng Lin, and Ian Reid. Learning depth from single monocular images using deep convolutional neural fields. *IEEE Trans. Pattern Anal. Mach. Intell.*, 38(10):2024–2039, 2015. 3
- [39] Ming-Yu Liu and Oncel Tuzel. Coupled generative adversarial networks. In *NIPS*, 2016. 4

- [40] Matthew Loper, Naureen Mahmood, Javier Romero, Gerard Pons-Moll, and Michael J. Black. SMPL: A skinned multi-person linear model. *ACM Trans. Graph.*, 34(6):1–16, 2015. 1
- [41] Andrew L. Maas, Awni Y. Hannun, and Andrew Y. Ng. Rectifier nonlinearities improve neural network acoustic models. In *ICML Workshop*, 2013. 23
- [42] Takeru Miyato, Toshiki Kataoka, Masanori Koyama, and Yuichi Yoshida. Spectral normalization for generative adversarial networks. In *ICLR*, 2018. 5, 23
- [43] Vinod Nair and Geoffrey E. Hinton. Rectified linear units improve restricted Boltzmann machines. In *ICML*, 2010. 23
- [44] Thu Nguyen-Phuoc, Chuan Li, Lucas Theis, Christian Richardt, and Yong-Liang Yang. HoloGAN: Unsupervised learning of 3D representations from natural images. In *ICCV*, 2019. 2, 3, 5, 6, 23
- [45] Maria-Elena Nilsback and Andrew Zisserman. Automated flower classification over a large number of classes. In *ICVGIP*, 2008. 2, 4, 5
- [46] Atsuhiko Noguchi and Tatsuya Harada. RGBD-GAN: Unsupervised 3D representation learning from natural image datasets via RGBD image synthesis. In *ICLR*, 2020. 2, 3, 6
- [47] Arthur Pajot, Emmanuel de Bezenac, and Patrick Gallinari. Unsupervised adversarial image reconstruction. In *ICLR*, 2018. 3
- [48] Ming Qian, Congyu Qiao, Jiamin Lin, Zhenyu Guo, Chenghua Li, Cong Leng, and Jian Cheng. BGGAN: Bokeh-glass generative adversarial network for rendering realistic bokeh. *arXiv preprint arXiv:2011.02242*, 2020. 3, 4
- [49] Olaf Ronneberger, Philipp Fischer, and Thomas Brox. U-net: Convolutional networks for biomedical image segmentation. In *MICCAI*, 2015. 24
- [50] Soubhik Sanyal, Timo Bolkart, Haiwen Feng, and Michael J. Black. Learning to regress 3D face shape and expression from an image without 3D supervision. In *CVPR*, 2019. 1, 3
- [51] Jiaxiang Shang, Tianwei Shen, Shiwei Li, Lei Zhou, Mingmin Zhen, Tian Fang, and Long Quan. Self-supervised monocular 3D face reconstruction by occlusion-aware multi-view geometry consistency. In *ECCV*, 2020. 1, 3
- [52] Xiaoyong Shen, Xin Tao, Hongyun Gao, Chao Zhou, and Jiaya Jia. Deep automatic portrait matting. In *ECCV*, 2016. 3
- [53] Pratul P. Srinivasan, Rahul Garg, Neal Wadhwa, Ren Ng, and Jonathan T. Barron. Aperture supervision for monocular depth estimation. In *CVPR*, 2018. 2, 3, 4, 23, 24
- [54] Attila Szabó, Givi Meishvili, and Paolo Favaro. Unsupervised generative 3D shape learning from natural images. *arXiv preprint arXiv:1910.00287*, 2019. 2, 3
- [55] Christian Szegedy, Vincent Vanhoucke, Sergey Ioffe, Jon Shlens, and Zbigniew Wojna. Rethinking the Inception architecture for computer vision. In *CVPR*, 2016. 5
- [56] Luan Tran and Xiaoming Liu. Nonlinear 3D face morphable model. In *CVPR*, 2018. 1, 3
- [57] Dmitry Ulyanov, Andrea Vedaldi, and Victor Lempitsky. Instance normalization: The missing ingredient for fast stylization. *arXiv preprint arXiv:1607.08022*, 2016. 5, 23
- [58] Carl Vondrick, Hamed Pirsiavash, and Antonio Torralba. Generating videos with scene dynamics. In *NIPS*, 2016. 3
- [59] Neal Wadhwa, Rahul Garg, David E. Jacobs, Bryan E. Feldman, Nori Kanazawa, Robert Carroll, Yair Movshovitz-Attias, Jonathan T. Barron, Yael Pritch, and Marc Levoy. Synthetic depth-of-field with a single-camera mobile phone. *ACM Trans. Graph.*, 37(4):1–13, 2018. 3
- [60] Catherine Wah, Steve Branson, Peter Welinder, Pietro Perona, and Serge Belongie. The Caltech-UCSD Birds-200-2011 Dataset. Technical Report CNS-TR-2011-001, California Institute of Technology, 2011. 2, 4, 5
- [61] Chaoyang Wang, José Miguel Buenaposada, Rui Zhu, and Simon Lucey. Learning depth from monocular videos using direct methods. In *CVPR*, 2018. 3
- [62] Lijun Wang, Xiaohui Shen, Jianming Zhang, Oliver Wang, Zhe Lin, Chih-Yao Hsieh, Sarah Kong, and Huchuan Lu. DeepLens: Shallow depth of field from a single image. *ACM Trans. Graph.*, 37(6):1–11, 2018. 3
- [63] Mengjiao Wang, Zhixin Shu, Shiyang Cheng, Yannis Panagakis, Dimitris Samaras, and Stefanos Zafeiriou. An adversarial neuro-tensorial approach for learning disentangled representations. *Int. J. Comput. Vis.*, 127(6-7):743–762, 2019. 1, 3
- [64] Xiaolong Wang and Abhinav Gupta. Generative image modeling using style and structure adversarial networks. In *ECCV*, 2016. 2
- [65] Zhou Wang, Alan C. Bovik, Hamid R. Sheikh, and Eero P. Simoncelli. Image quality assessment: From error visibility to structural similarity. *IEEE Trans. Image Process.*, 13(4):600–612, 2004. 11
- [66] Jiajun Wu, Chengkai Zhang, Tianfan Xue, Bill Freeman, and Josh Tenenbaum. Learning a probabilistic latent space of object shapes via 3D generative-adversarial modeling. In *NIPS*, 2016. 2
- [67] Shangzhe Wu, Christian Rupprecht, and Andrea Vedaldi. Unsupervised learning of probably symmetric deformable 3D objects from images in the wild. In *CVPR*, 2020. 2, 3
- [68] Ke Xian, Jianming Zhang, Oliver Wang, Long Mai, Zhe Lin, and Zhiguo Cao. Structure-guided ranking loss for single image depth prediction. In *CVPR*, 2020. 3, 5, 6, 20
- [69] Bing Xu, Naiyan Wang, Tianqi Chen, and Mu Li. Empirical evaluation of rectified activations in convolutional network. In *ICML Workshop*, 2015. 23
- [70] Dan Xu, Elisa Ricci, Wanli Ouyang, Xiaogang Wang, and Nicu Sebe. Multi-scale continuous CRFs as sequential deep networks for monocular depth estimation. In *CVPR*, 2017. 3
- [71] Jianwei Yang, Anitha Kannan, Dhruv Batra, and Devi Parikh. LR-GAN: Layered recursive generative adversarial networks for image generation. In *ICLR*, 2017. 3
- [72] Zhichao Yin and Jianping Shi. GeoNet: Unsupervised learning of dense depth, optical flow and camera pose. In *CVPR*, 2018. 3
- [73] Richard Zhang, Phillip Isola, Alexei A. Efros, Eli Shechtman, and Oliver Wang. The unreasonable effectiveness of deep features as a perceptual metric. In *CVPR*, 2018. 6, 11, 12
- [74] Shengyu Zhao, Zhijian Liu, Ji Lin, Jun-Yan Zhu, and Song Han. Differentiable augmentation for data-efficient GAN training. In *NeurIPS*, 2020. 24
- [75] Tinghui Zhou, Matthew Brown, Noah Snavely, and David G. Lowe. Unsupervised learning of depth and ego-motion from video. In *CVPR*, 2017. 3
- [76] Jun-Yan Zhu, Taesung Park, Phillip Isola, and Alexei A. Efros. Unpaired image-to-image translation using cycle-consistent adversarial networks. In *ICCV*, 2017. 3, 4, 8

Appendix

In this appendix, we provide further analyses (Appendix A), extended results (Appendix B), and implementation details (Appendix C) regarding our study.

A. Further analyses

In this section, we provide three additional analyses for a deeper understanding of metrics and the proposed model.

- Appendix A.1: Further analysis of metrics.
- Appendix A.2: Further analysis of DoF mixture learning. This is a detailed analysis of the experiments presented in Section 5.3.1.
- Appendix A.3: Further analysis of the center focus prior. This is a detailed analysis of the experiments presented in Section 5.3.2.

A.1. Further analysis of metrics

As discussed in Section 5.1, because of our objective and formulation, that is, learning an unconditional model from unpaired and unlabeled natural images, it is nontrivial to prepare the ground truth or construct a metric that can measure depth and DoF accuracy directly. As alternatives, in the ablation study (Section 5.3), we adopted two metrics: *learned perceptual image patch similarity (LPIPS)* [73] and *depth standard deviation (DSD)*, along with *kernel inception distance (KID)* [2] and *scale-invariant depth error (SIDE)* [9]. For further clarification, in this subsection, we first evaluate the performance of three additional metrics along with the aforementioned metrics (Section A.1.1), and then discuss their relationships (Section A.1.2).

A.1.1 Evaluation on additional metrics

Additional metrics. We adopted three additional metrics.

(1) *Structural similarity index measure (SSIM)* [65]. SSIM is a representative traditional (or non-DNN-based) metric for predicting perceived quality. This metric measures the distance between two images; a larger value indicates higher similarity. SSIM is a possible alternative to LPIPS, which was used in Section 5.3. The reason for using LPIPS is that a previous study [73] demonstrated that LPIPS has a higher correlation with human perceptual judgments than SSIM. We consider this characteristic to be useful for measuring the validity of the DoF effect where, between deep and shallow DoF images, the appearance of focused targets is nearly similar, but that of unfocused regions is relatively different. To validate this consideration, we will compare LPIPS and SSIM later.

(2) $KID_{I_s^g}$. We calculated the KID score between *all real* images (i.e., $I^r \sim p^r(I)$) and *generated shallow DoF* images (i.e., $I_s^g = R(G_I(z), G_D(z))$, where $z \sim p(z)$). When I^r includes both deep (i.e., $I_d^r \sim p^r(I_d)$) and shallow (i.e.,

$I_s^r \sim p^r(I_s)$) DoF images, it is expected that $KID_{I_s^g}$ is moderately small but larger than KID, which measures the distance between *all real* (i.e., $I^r \sim p^r(I)$) images and *all generated* images (i.e., $I^g \sim p^g(I)$).¹⁰

(3) $KID_{I_d^g}$. We computed the KID score between *all real* images (i.e., $I^r \sim p^r(I)$) and *generated deep DoF* images (i.e., $I_d^g = G_I(z)$, where $z \sim p(z)$). This metric has a similar characteristic as $KID_{I_s^g}$.

Results. We applied the aforementioned metrics to the models presented in Table 3. Table 5 summarizes the results. Our main findings are three-fold:

(1) *Comparison of KID, $KID_{I_s^g}$, and $KID_{I_d^g}$ among AR-GANs with different p_s (Nos. 1–5).* We found that as p_s (i.e., the probability that a shallow DoF image is rendered) decreases, $KID_{I_s^g}$ increases and $KID_{I_d^g}$ decreases. In particular, when comparing $KID_{I_s^g}$ and $KID_{I_d^g}$, the KID for the dominant image (i.e., one used at a higher frequency in training) obtains a smaller value than the KID for the non-dominant image. The KID for the non-dominant image is also moderately small when the image is used in training (i.e., $p_s \in \{0.75, 0.5, 0.25\}$ (Nos. 2–4)). By contrast, when either I_s^g or I_d^g is used for training (i.e., $p_s \in \{1, 0\}$ (Nos. 1 and 5)), the KID for the unused one is relatively high. These results imply that DoF mixture learning is useful for matching both $p^g(I_d)$ and $p^g(I_s)$ with parts of the real distribution, which are expected to be $p^r(I_d)$ and $p^r(I_s)$, respectively.

(2) *Comparison of KID, $KID_{I_s^g}$, and $KID_{I_d^g}$ between AR-GANs with different learning methods (Nos. 6 and 7).* When an explicit distance metric (L1 in this experiment (No. 6)) is used, it is encouraged to compare generated deep DoF images (i.e., I_d^g) with generated shallow DoF images (i.e., I_s^g). However, an adversarial loss is imposed only on I_s^g ; consequently, its $KID_{I_d^g}$ is significantly larger than that of AR-GANs with DoF mixture learning (Nos. 2–4). This suggests that, in this case, the visual fidelity of I_d^g may not be high, even when the LPIPS is small.

When the double discriminators (No. 7) are used, both $KID_{I_s^g}$ and $KID_{I_d^g}$ approach KID. This result indicates that both $p^g(I_s)$ and $p^g(I_d)$ are encouraged to coincide with the overall real distribution $p^r(I)$, which consists of $p^r(I_s)$ and $p^r(I_d)$. This phenomenon can also be explained by the fact that LPIPS and DSD are almost 0, and SSIM is close to 1.

From these results, we conclude that DoF mixture learning is more reasonable than L1 and double discriminators when a dataset includes both deep and shallow DoF images (Assumption 1), and we aim to selectively represent the real image distribution according to the DoF strength.

(3) *Comparison of LPIPS and SSIM.* In most cases, as LPIPS decreases, SSIM increases. We would like to note that the similarity is higher when the LPIPS value is small,

¹⁰When calculating KID for AR-GANs, we used the DoF mixture setting that was used in training. Therefore, in Table 3, the rates of I_d^g and I_s^g that were used to calculate the KID vary according to the model.

(a) Oxford Flowers								
No.	Learning method	KID $\times 10^3\downarrow$	KID $I_s^g \times 10^3\downarrow$	KID $I_d^g \times 10^3\downarrow$	SIDE $\times 10^2\downarrow$	LPIPS \downarrow	SSIM \uparrow	DSD \uparrow
1	I_s^g only $p_s = 1$	12.36 ± 0.59	12.46 ± 0.58	293.56 ± 44.92	5.48 ± 0.20	0.229 ± 0.027	0.406 ± 0.049	0.157 ± 0.063
2	Mixture $p_s = 0.75$	10.97 ± 0.26	13.74 ± 0.47	26.50 ± 1.59	4.81 ± 0.06	0.023 ± 0.001	0.943 ± 0.002	0.657 ± 0.006
3	Mixture $p_s = 0.5$	10.69 ± 0.48	18.98 ± 1.24	17.58 ± 0.53	4.65 ± 0.05	0.022 ± 0.000	0.940 ± 0.002	0.771 ± 0.022
4	Mixture $p_s = 0.25$	11.23 ± 0.36	30.61 ± 2.99	12.91 ± 0.38	4.46 ± 0.03	0.028 ± 0.001	0.919 ± 0.002	1.007 ± 0.025
5	I_d^g only $p_s = 0$	11.58 ± 0.37	36.63 ± 5.11	11.51 ± 0.41	4.56 ± 0.20	0.113 ± 0.013	0.870 ± 0.020	0.446 ± 0.065
6	L1	11.66 ± 0.72	11.81 ± 0.74	47.59 ± 2.54	5.26 ± 0.65	0.033 ± 0.001	0.932 ± 0.002	0.387 ± 0.116
7	Double discriminators	9.74 ± 0.31	9.79 ± 0.38	9.88 ± 0.30	6.79 ± 2.21	0.000 ± 0.001	0.999 ± 0.001	0.032 ± 0.046
(b) CUB-200-2011								
No.	Learning method	KID $\times 10^3\downarrow$	KID $I_s^g \times 10^3\downarrow$	KID $I_d^g \times 10^3\downarrow$	SIDE $\times 10^2\downarrow$	LPIPS \downarrow	SSIM \uparrow	DSD \uparrow
1	I_s^g only $p_s = 1$	13.62 ± 0.53	13.71 ± 0.58	72.63 ± 25.71	4.63 ± 0.50	0.125 ± 0.037	0.786 ± 0.029	0.354 ± 0.021
2	Mixture $p_s = 0.75$	12.68 ± 0.61	12.30 ± 0.45	22.64 ± 0.37	3.75 ± 0.08	0.037 ± 0.003	0.921 ± 0.006	0.748 ± 0.072
3	Mixture $p_s = 0.5$	13.14 ± 0.03	13.20 ± 0.43	18.15 ± 0.07	3.55 ± 0.02	0.043 ± 0.003	0.909 ± 0.007	0.959 ± 0.075
4	Mixture $p_s = 0.25$	14.30 ± 0.56	18.28 ± 0.73	16.19 ± 0.63	3.58 ± 0.04	0.059 ± 0.002	0.877 ± 0.003	1.175 ± 0.017
5	I_d^g only $p_s = 0$	14.58 ± 0.56	28.63 ± 2.14	14.85 ± 0.72	5.94 ± 0.70	0.115 ± 0.019	0.908 ± 0.010	0.193 ± 0.012
6	L1	12.54 ± 0.32	12.59 ± 0.45	33.70 ± 0.84	5.75 ± 1.26	0.042 ± 0.001	0.910 ± 0.001	0.725 ± 0.195
7	Double discriminators	12.50 ± 0.12	12.56 ± 0.20	12.61 ± 0.29	4.33 ± 0.34	0.000 ± 0.000	1.000 ± 0.000	0.001 ± 0.000
(c) FFHQ								
No.	Learning method	KID $\times 10^3\downarrow$	KID $I_s^g \times 10^3\downarrow$	KID $I_d^g \times 10^3\downarrow$	SIDE $\times 10^2\downarrow$	LPIPS \downarrow	SSIM \uparrow	DSD \uparrow
1	I_s^g only $p_s = 1$	5.75 ± 0.44	5.82 ± 0.48	74.36 ± 7.41	6.00 ± 0.35	0.097 ± 0.011	0.808 ± 0.034	0.296 ± 0.018
2	Mixture $p_s = 0.75$	5.67 ± 0.23	6.05 ± 0.14	14.50 ± 0.65	4.38 ± 0.10	0.009 ± 0.001	0.967 ± 0.006	0.757 ± 0.177
3	Mixture $p_s = 0.5$	5.75 ± 0.19	7.53 ± 0.43	9.34 ± 0.22	4.21 ± 0.15	0.009 ± 0.001	0.966 ± 0.006	0.769 ± 0.119
4	Mixture $p_s = 0.25$	6.17 ± 0.08	11.55 ± 0.70	7.53 ± 0.41	4.68 ± 0.33	0.010 ± 0.001	0.968 ± 0.004	0.583 ± 0.071
5	I_d^g only $p_s = 0$	6.85 ± 0.13	10.16 ± 0.29	6.94 ± 0.10	4.77 ± 0.13	0.028 ± 0.006	0.976 ± 0.003	0.202 ± 0.003
6	L1	5.82 ± 0.21	5.83 ± 0.23	24.89 ± 2.70	4.82 ± 0.09	0.015 ± 0.004	0.967 ± 0.005	0.466 ± 0.045
7	Double discriminators	6.20 ± 0.08	6.26 ± 0.06	6.19 ± 0.07	5.20 ± 0.47	0.000 ± 0.000	1.000 ± 0.000	0.000 ± 0.000

Table 5. **Comparison of KID $\times 10^3\downarrow$, KID $I_s^g \times 10^3\downarrow$, KID $I_d^g \times 10^3\downarrow$, SIDE $\times 10^2\downarrow$, LPIPS \downarrow , SSIM \uparrow , and DSD \uparrow among AR-GANs with different learning methods.** This is an extended version of Table 3.

as well as when the SSIM value is large. However, in some cases (for example, between Nos. 4 and 5 in CUB-200-2011), this tendency does not hold. We discuss this in Appendix A.1.2.

A.1.2 Relationships among metrics

In the results in Table 5, there are two nontrivial relationships among metrics: (1) *relationship between LPIPS and DSD*, and (2) *relationship between LPIPS and SSIM*. Next, we discuss the two relationships with examples.

(1) *Relationship between LPIPS and DSD*. Figure 10 shows the relationship between LPIPS and DSD. We selected three representative models based on the results in Table 5(a): (a) *AR-GAN with double discriminators* (No. 7), for which the LPIPS and DSD are small, (b) *AR-GAN with DoF mixture learning at $p_s = 0.25$* (No. 4), for which the LPIPS is small and the DSD is large, and (c) *AR-GAN with I_s^g only* (No. 1), for which the LPIPS is large and the DSD is small.

As shown in this figure, when the DSD is small (a, c), the model fails to learn the depth (i.e., the depth is almost constant). By contrast, when the DSD is large (b), the model succeeds in learning the meaningful depth. Furthermore, when the LPIPS is small (a, b), the content is preserved between the deep and shallow DoF images. By contrast, when the LPIPS is large (c), the deep DoF image is corrupted. As

described, LPIPS and DSD reflect the success and failure of the learning of the depth and DoF effect reasonably well. Therefore, we believe that they are reasonable metrics for this task.

(2) *Relationship between LPIPS and SSIM*. Figure 11 shows the relationship between LPIPS and SSIM. We selected four representative models based on the results in Table 5(b): (a) *AR-GAN with double discriminators* (No. 7), in which deep and shallow DoF images are similar in terms of both LPIPS and SSIM, (b) *AR-GAN with DoF mixture learning at $p_s = 0.25$* (No. 4), in which deep and shallow DoF images are similar in terms of LPIPS but dissimilar in terms of SSIM, (c) *AR-GAN with I_d^g only* (No. 5), in which deep and shallow DoF images are similar in terms of SSIM but dissimilar in terms of LPIPS, and (d) *AR-GAN with I_s^g only* (No. 1), in which deep and shallow DoF images are dissimilar in terms of both LPIPS and SSIM.

As shown in this figure, LPIPS is sensitive to overall blur (c), in which both the main object and its surroundings are blurred.¹¹ However, it is insensitive to center focus blur (b), in which the main object in focus is not blurred but the surrounding area is blurred. By contrast, SSIM is sensitive to the center focus blur (b) but insensitive to the overall blur (c). This is because LPIPS measures the distance based on

¹¹This tendency has also been observed in the original study on LPIPS [73].

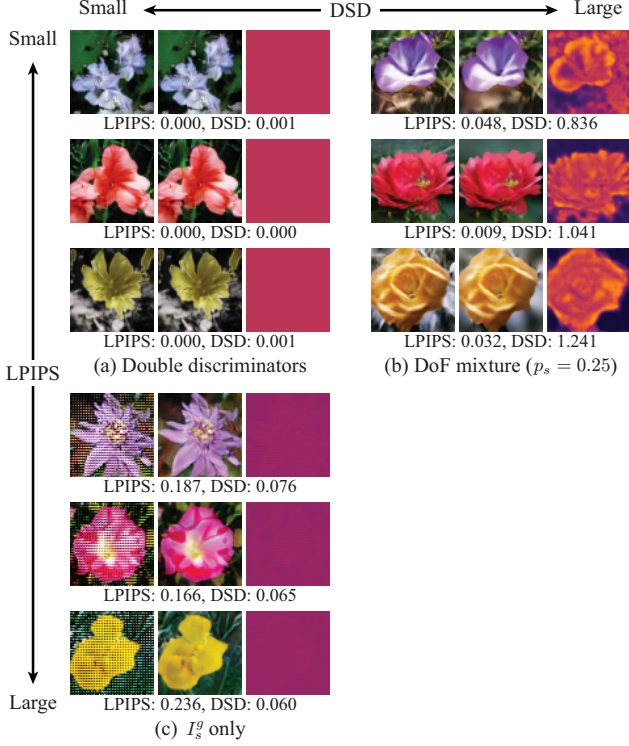


Figure 10. **Relationship between LPIPS and DSD.** In each block (a–c), the three images in the rows represent the generated deep DoF image (i.e., I_d^g), shallow DoF image (i.e., I_s^g), and depth (i.e., D^g), from left to right. The three images in the columns were generated from different noise z . For ease of viewing, the depth was normalized using the same values across all results. The models were trained using Oxford Flowers.

the classifier that is sensitive to the difference in the main target but insensitive to the differences in the irrelevant surroundings. Our objective is to learn the natural DoF effect, in which the main target and the surroundings tend to be unchanged and changed, respectively, before and after defocusing. To achieve this objective, we believe that LPIPS is more appropriate than SSIM as a metric that measures the unexpected dissimilarity caused by factors other than the DoF effect.

A.2. Further analysis of DoF mixture learning

A.2.1 Effect of sampling methods

As described in Section 4.3, we sampled s (Equation 6) from a binomial distribution, which is $p(s) = B(1, p_s)$. As demonstrated in the experiments in Section 5, this setting works reasonably well. However, as a further analysis, in this subsection, we evaluate the performance when s is sampled from a different distribution, particularly a uniform distribution, which is $p(s) = U(0, 1)$.

Results. Table 6 summarizes the comparison of KID, $KID_{I_s^g}$, $KID_{I_d^g}$, SIDE, LPIPS, and DSD among AR-GANs with different sampling methods. When a binomial distri-

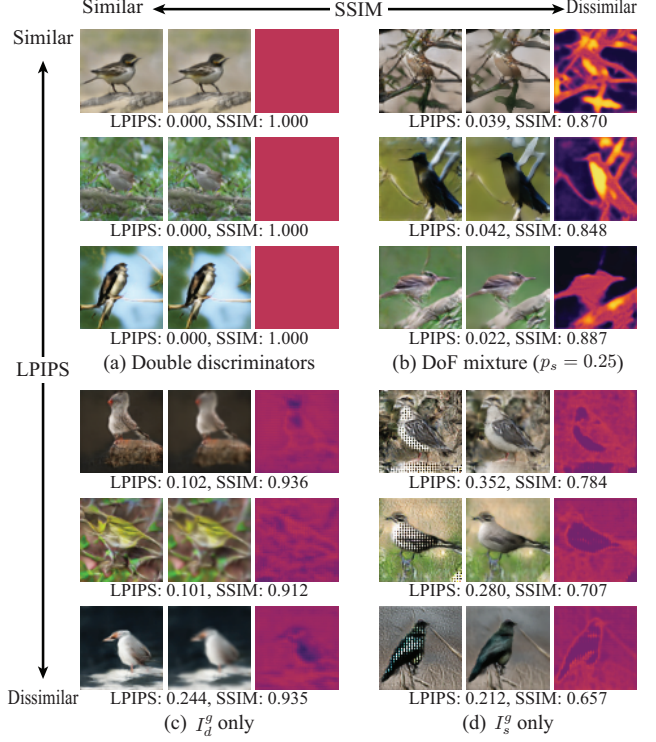


Figure 11. **Relationship between LPIPS and SSIM.** In each block (a–d), the three images in the rows represent the generated deep DoF image (i.e., I_d^g), shallow DoF image (i.e., I_s^g), and depth (i.e., D^g), from left to right. The three images in the columns were generated from different noise z . For ease of viewing, the depth was normalized using the same values across all results. The models were trained using CUB-200-2011.

bution is used (i.e., $s \in \{0, 1\}$), the relationship between the deep and shallow DoF images is discretely represented. By contrast, when a uniform distribution is used (i.e., $s \in [0, 1]$), the relationship is continuously represented. In the latter case, deep and shallow DoF images are represented continuously, and their total distribution is encouraged to represent the overall real distribution. Therefore, I_d^g ($s = 0$) represents the deepest DoF image, and I_s^g ($s = 1$) represents the most shallow DoF image among the various DoF images. Consequently, the difference between I_d^g and I_s^g becomes larger compared with the use of a binomial distribution. Therefore, in Table 6, the LPIPS for $U(0, 1)$ (No. 6) is larger than those for $B(1, p_s)$ at $p_s \in \{0.25, 0.5, 0.75\}$ (Nos. 2–4) and the DSD for $U(0, 1)$ (No. 6) is comparable with those for $B(1, p_s)$, which achieved the largest DSD among Nos. 2–4. Because of this characteristic difference, there are advantages and disadvantages for both a uniform distribution and a binomial distribution. The choice of sampling methods is therefore task-specific.

A.2.2 Comparison with another alternative learning

In Section 5.3.1, we tested *L1* and *double discriminators* as possible alternatives to DoF mixture learning. As a further

(a) Oxford Flowers

No.	Sampling method	KID $\times 10^3\downarrow$	KID $_{I_s^g}\times 10^3\downarrow$	KID $_{I_d^g}\times 10^3\downarrow$	SIDE $\times 10^2\downarrow$	LPIPS \downarrow	DSD \uparrow
1	I_s^g only $B(1, 1)$	12.36 \pm 0.59	12.46 \pm 0.58	293.56 \pm 44.92	5.48 \pm 0.20	0.229 \pm 0.027	0.157 \pm 0.063
2	Mixture $B(1, 0.75)$	10.97 \pm 0.26	13.74 \pm 0.47	26.50 \pm 1.59	4.81 \pm 0.06	0.023 \pm 0.001	0.657 \pm 0.006
3	Mixture $B(1, 0.5)$	10.69 \pm 0.48	18.98 \pm 1.24	17.58 \pm 0.53	4.65 \pm 0.05	0.022 \pm 0.000	0.771 \pm 0.022
4	Mixture $B(1, 0.25)$	11.23 \pm 0.36	30.61 \pm 2.99	12.91 \pm 0.38	4.46 \pm 0.03	0.028 \pm 0.001	1.007 \pm 0.025
5	I_d^g only $B(1, 0)$	11.58 \pm 0.37	36.63 \pm 5.11	11.51 \pm 0.41	4.56 \pm 0.20	0.113 \pm 0.013	0.446 \pm 0.065
6	Mixture $U(0, 1)$	10.67 \pm 0.16	21.14 \pm 2.49	29.72 \pm 0.80	4.31 \pm 0.11	0.040 \pm 0.002	0.857 \pm 0.118

(b) CUB-200-2011

No.	Sampling method	KID $\times 10^3\downarrow$	KID $_{I_s^g}\times 10^3\downarrow$	KID $_{I_d^g}\times 10^3\downarrow$	SIDE $\times 10^2\downarrow$	LPIPS \downarrow	DSD \uparrow
1	I_s^g only $B(1, 1)$	13.62 \pm 0.53	13.71 \pm 0.58	72.63 \pm 25.71	4.63 \pm 0.50	0.125 \pm 0.037	0.354 \pm 0.021
2	Mixture $B(1, 0.75)$	12.68 \pm 0.61	12.30 \pm 0.45	22.64 \pm 0.37	3.75 \pm 0.08	0.037 \pm 0.003	0.748 \pm 0.072
3	Mixture $B(1, 0.5)$	13.14 \pm 0.03	13.20 \pm 0.43	18.15 \pm 0.07	3.55 \pm 0.02	0.043 \pm 0.003	0.959 \pm 0.075
4	Mixture $B(1, 0.25)$	14.30 \pm 0.56	18.28 \pm 0.73	16.19 \pm 0.63	3.58 \pm 0.04	0.059 \pm 0.002	1.175 \pm 0.017
5	I_d^g only $B(1, 0)$	14.58 \pm 0.56	28.63 \pm 2.14	14.85 \pm 0.72	5.94 \pm 0.70	0.115 \pm 0.019	0.193 \pm 0.012
6	Mixture $U(0, 1)$	12.43 \pm 0.92	13.38 \pm 0.70	25.60 \pm 1.89	3.62 \pm 0.04	0.072 \pm 0.006	1.142 \pm 0.038

(c) FFHQ

No.	Sampling method	KID $\times 10^3\downarrow$	KID $_{I_s^g}\times 10^3\downarrow$	KID $_{I_d^g}\times 10^3\downarrow$	SIDE $\times 10^2\downarrow$	LPIPS \downarrow	DSD \uparrow
1	I_s^g only $B(1, 1)$	5.75 \pm 0.44	5.82 \pm 0.48	74.36 \pm 7.41	6.00 \pm 0.35	0.097 \pm 0.011	0.296 \pm 0.018
2	Mixture $B(1, 0.75)$	5.67 \pm 0.23	6.05 \pm 0.14	14.50 \pm 0.65	4.38 \pm 0.10	0.009 \pm 0.001	0.757 \pm 0.177
3	Mixture $B(1, 0.5)$	5.75 \pm 0.19	7.53 \pm 0.43	9.34 \pm 0.22	4.21 \pm 0.15	0.009 \pm 0.001	0.769 \pm 0.119
4	Mixture $B(1, 0.25)$	6.17 \pm 0.08	11.55 \pm 0.70	7.53 \pm 0.41	4.68 \pm 0.33	0.010 \pm 0.001	0.583 \pm 0.071
5	I_d^g only $B(1, 0)$	6.85 \pm 0.13	10.16 \pm 0.29	6.94 \pm 0.10	4.77 \pm 0.13	0.028 \pm 0.006	0.202 \pm 0.003
6	Mixture $U(0, 1)$	5.86 \pm 0.06	7.30 \pm 0.02	17.86 \pm 0.25	4.49 \pm 0.09	0.020 \pm 0.001	1.130 \pm 0.085

Table 6. Comparison of KID $\times 10^3\downarrow$, KID $_{I_s^g}\times 10^3\downarrow$, KID $_{I_d^g}\times 10^3\downarrow$, SIDE $\times 10^2\downarrow$, LPIPS \downarrow , and DSD \uparrow among AR-GANs with different sampling methods.

(a) Oxford Flowers

No.	Distance metric	KID $\times 10^3\downarrow$	KID $_{I_s^g}\times 10^3\downarrow$	KID $_{I_d^g}\times 10^3\downarrow$	SIDE $\times 10^2\downarrow$	LPIPS \downarrow	DSD \uparrow
1	L1	11.66 \pm 0.72	11.81 \pm 0.74	47.59 \pm 2.54	5.26 \pm 0.65	0.033 \pm 0.001	0.387 \pm 0.116
2	Perceptual loss	11.18 \pm 0.52	11.33 \pm 0.58	40.35 \pm 0.56	4.70 \pm 0.06	0.028 \pm 0.001	0.589 \pm 0.041

(b) CUB-200-2011

No.	Distance metrics	KID $\times 10^3\downarrow$	KID $_{I_s^g}\times 10^3\downarrow$	KID $_{I_d^g}\times 10^3\downarrow$	SIDE $\times 10^2\downarrow$	LPIPS \downarrow	DSD \uparrow
1	L1	12.54 \pm 0.32	12.59 \pm 0.45	33.70 \pm 0.84	5.75 \pm 1.26	0.042 \pm 0.001	0.725 \pm 0.195
2	Perceptual loss	12.78 \pm 0.21	12.82 \pm 0.23	36.16 \pm 2.34	3.75 \pm 0.07	0.054 \pm 0.003	0.754 \pm 0.053

(c) FFHQ

No.	Distance metric	KID $\times 10^3\downarrow$	KID $_{I_s^g}\times 10^3\downarrow$	KID $_{I_d^g}\times 10^3\downarrow$	SIDE $\times 10^2\downarrow$	LPIPS \downarrow	DSD \uparrow
1	L1	5.82 \pm 0.21	5.83 \pm 0.23	24.89 \pm 2.70	4.82 \pm 0.09	0.015 \pm 0.004	0.466 \pm 0.045
2	Perceptual loss	5.64 \pm 0.40	5.66 \pm 0.42	39.37 \pm 1.46	5.31 \pm 0.07	0.024 \pm 0.002	0.439 \pm 0.010

Table 7. Comparison of KID $\times 10^3\downarrow$, KID $_{I_s^g}\times 10^3\downarrow$, KID $_{I_d^g}\times 10^3\downarrow$, SIDE $\times 10^2\downarrow$, LPIPS \downarrow , and DSD \uparrow between AR-GANs using different distance metrics. Refer to Table 5 for a comparison with the results of other learning methods.

alternative, we test *perceptual loss* [23, 8], which is a variant of explicit distance metrics and measures the distance between two images in the CNN feature space. Recent studies [8, 34] have shown that perceptual loss is more useful than pixel-level metrics (e.g., L1 and L2) when aiming to improve visual fidelity.

Results. Table 7 summarizes the comparison of KID, KID $_{I_s^g}$, KID $_{I_d^g}$, SIDE, LPIPS, and DSD between AR-GANs using different distance metrics. We found that even when using perceptual loss (No. 2), explicit distance metric-based methods (Nos. 1 and 2) find it difficult to improve both the LPIPS and DSD simultaneously. Furthermore, they also

find it difficult to improve KID $_{I_d^g}$. It is noteworthy that DoF mixture learning can address these difficulties, as listed in Table 5 and discussed in Appendix A.1.1. These results indicate that the aforementioned difficulties are common in explicit distance metric-based methods, including L1 and perceptual loss.

A.3. Further analysis of center focus prior

A.3.1 Effect of duration of using center focus prior

In Section 5.3.2, we used the center focus prior only at the beginning of training to mitigate the negative effect caused by the gap between the real depth and the predefined center

(a) Oxford Flowers							
No.	Usage of prior	$KID \times 10^3 \downarrow$	$KID_{I_s^g} \times 10^3 \downarrow$	$KID_{I_d^g} \times 10^3 \downarrow$	$SIDE \times 10^2 \downarrow$	$LPIPS \downarrow$	$DSD \uparrow$
1	W/ D_p at beginning	11.23 ± 0.36	30.61 ± 2.99	12.91 ± 0.38	4.46 ± 0.03	0.028 ± 0.001	1.007 ± 0.025
2	W/ D_p until end	10.98 ± 0.27	29.33 ± 0.52	12.70 ± 0.50	4.54 ± 0.01	0.019 ± 0.001	0.259 ± 0.001
3	W/o D_p	10.69 ± 0.24	27.79 ± 2.50	12.60 ± 0.23	6.78 ± 1.58	0.026 ± 0.002	0.915 ± 0.137
(b) CUB-200-2011							
No.	Usage of prior	$KID \times 10^3 \downarrow$	$KID_{I_s^g} \times 10^3 \downarrow$	$KID_{I_d^g} \times 10^3 \downarrow$	$SIDE \times 10^2 \downarrow$	$LPIPS \downarrow$	$DSD \uparrow$
1	W/ D_p at beginning	14.30 ± 0.56	18.28 ± 0.73	16.19 ± 0.63	3.58 ± 0.04	0.059 ± 0.002	1.175 ± 0.017
2	W/ D_p until end	13.96 ± 0.76	16.71 ± 1.06	15.11 ± 0.95	5.29 ± 0.02	0.034 ± 0.000	0.250 ± 0.001
3	W/o D_p	13.96 ± 0.63	17.40 ± 1.01	16.01 ± 0.66	4.86 ± 1.84	0.062 ± 0.004	1.183 ± 0.059
(c) FFHQ							
No.	Usage of prior	$KID \times 10^3 \downarrow$	$KID_{I_s^g} \times 10^3 \downarrow$	$KID_{I_d^g} \times 10^3 \downarrow$	$SIDE \times 10^2 \downarrow$	$LPIPS \downarrow$	$DSD \uparrow$
1	W/ D_p at beginning	5.75 ± 0.19	7.53 ± 0.43	9.34 ± 0.22	4.21 ± 0.15	0.009 ± 0.001	0.769 ± 0.119
2	W/ D_p until end	5.67 ± 0.17	7.98 ± 0.36	9.06 ± 0.22	4.31 ± 0.04	0.008 ± 0.001	0.271 ± 0.004
3	W/o D_p	5.72 ± 0.10	7.78 ± 0.51	9.88 ± 0.32	6.70 ± 1.88	0.009 ± 0.001	0.851 ± 0.057

Table 8. **Comparison of $KID \times 10^3 \downarrow$, $KID_{I_s^g} \times 10^3 \downarrow$, $KID_{I_d^g} \times 10^3 \downarrow$, $SIDE \times 10^2 \downarrow$, $LPIPS \downarrow$, and $DSD \uparrow$ among AR-GANs with and without center focus prior.** The duration of the center focus prior usage changes between W/ D_p at the beginning (No. 1) and W/ D_p until the end (No. 2). This is an extended version of Table 4.

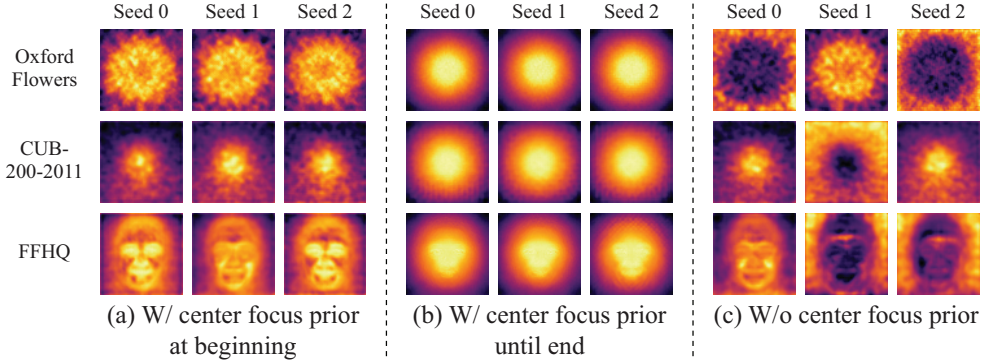


Figure 12. **Comparison of AD with and without D_p .** This is an extended version of Figure 7. Light color indicates the foreground.

focus prior. To validate this strategy, we evaluated the performance of the model that used the center focus prior until the end of training.

Results. Table 8 summarizes the comparison of KID , $KID_{I_s^g}$, $KID_{I_d^g}$, $SIDE$, $LPIPS$, and DSD among AR-GANs with and without center focus prior. Specifically, we changed the duration of the center focus prior usage between w/ D_p at beginning (No. 1) and w/ D_p until end (No. 2). As discussed in Section 5.3.2, when D_p is used only at the beginning of the training (No. 1), the score differences between the models with and without D_p (Nos. 1 and 3) are relatively small. However, when D_p is used until the end of the training (No. 2), the DSD is significantly smaller than the results without D_p (No. 3). These results indicate that when D_p is used until the end of the training, the depth learning is disturbed, but when its usage is stopped in the early phase of training, learning is not prevented.

As further evidence, we show a comparison of the average depth (AD) in Figure 12. As shown here, when D_p is used only at the beginning of the training (a), AD is deformed depending on the dataset. However, when D_p is used until the end of the training (b), AD is almost the same

as the center focus prior shown in Figure 4(b). These results also support the aforementioned statement that when D_p is used until the end of the training, the depth learning is disturbed.

B. Extended results

In this appendix, we provide extended versions of the figures presented in the main text. Figure titles and the relationships with the figures presented in the main text are as follows:

- Figure 13: Unsupervised learning of depth and DoF effect from unlabeled natural images. This is an extended version of Figure 1.
- Figure 14: Linear interpolation in the latent space of the AR-GAN generator. This is an extended version of Figure 1.
- Figure 15: Qualitative comparison among HoloGAN, RGBD-GAN, and AR-GAN. This is an extended version of Figure 5.
- Figure 16: Examples of predicted depths. This is an extended version of Figure 6.
- Figure 17: Examples of data generated using AR-HoloGAN and AR-RGBD-GAN. This is an extended version of Figure 8.
- Figure 18: Examples of shallow DoF rendering. This is an extended version of Figure 9.



Figure 13. **Unsupervised learning of depth and DoF effect from unlabeled natural images.** This is an extended version of Figure 1. Once trained, our model can synthesize tuples of deep and shallow DoF images and depths from random noise. Here, we show the results generated using AR-GANs trained with 128×128 images. The three images in each image block represent the generated deep DoF image (i.e., I_d^g), shallow DoF image (i.e., I_s^g), and depth (i.e., D^g), from left to right. The images in the columns are generated from different noise (i.e., z).

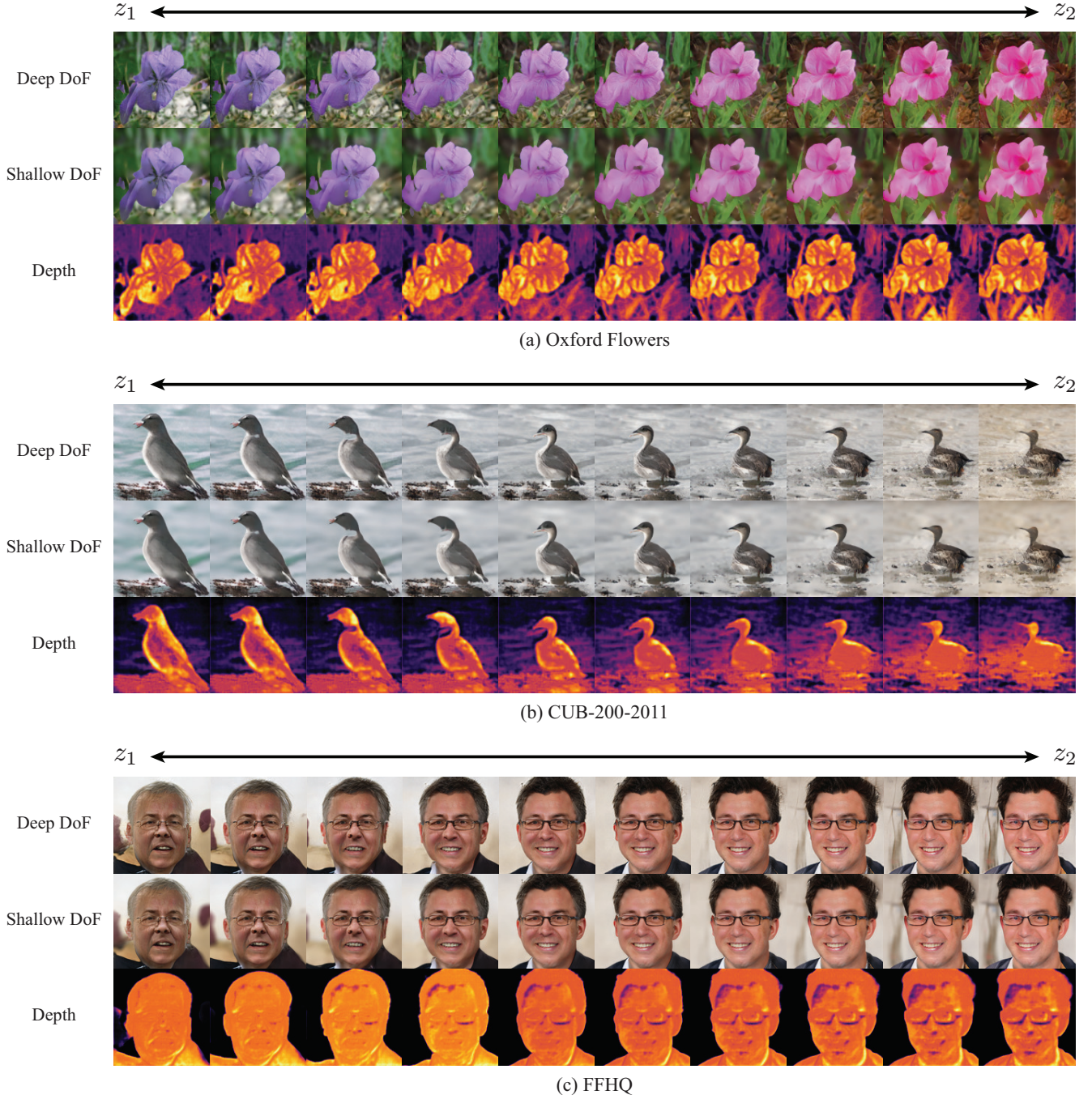


Figure 14. **Linear interpolation in the latent space of the AR-GAN generator.** This is an extended version of Figure 1. In the horizontal direction, we linearly interpolated the noise $z \in [z_1, z_2]$ in the latent space of the AR-GAN generator. The three images in the columns represent the deep DoF image (i.e., I_d^g), shallow DoF image (i.e., I_s^g), and depth (i.e., D^g) that were generated from the corresponding noise z , from top to bottom. As shown here, AR-GANs can manipulate the contents of tuples of (I_s^g, I_d^g, D^g) continuously according to z .

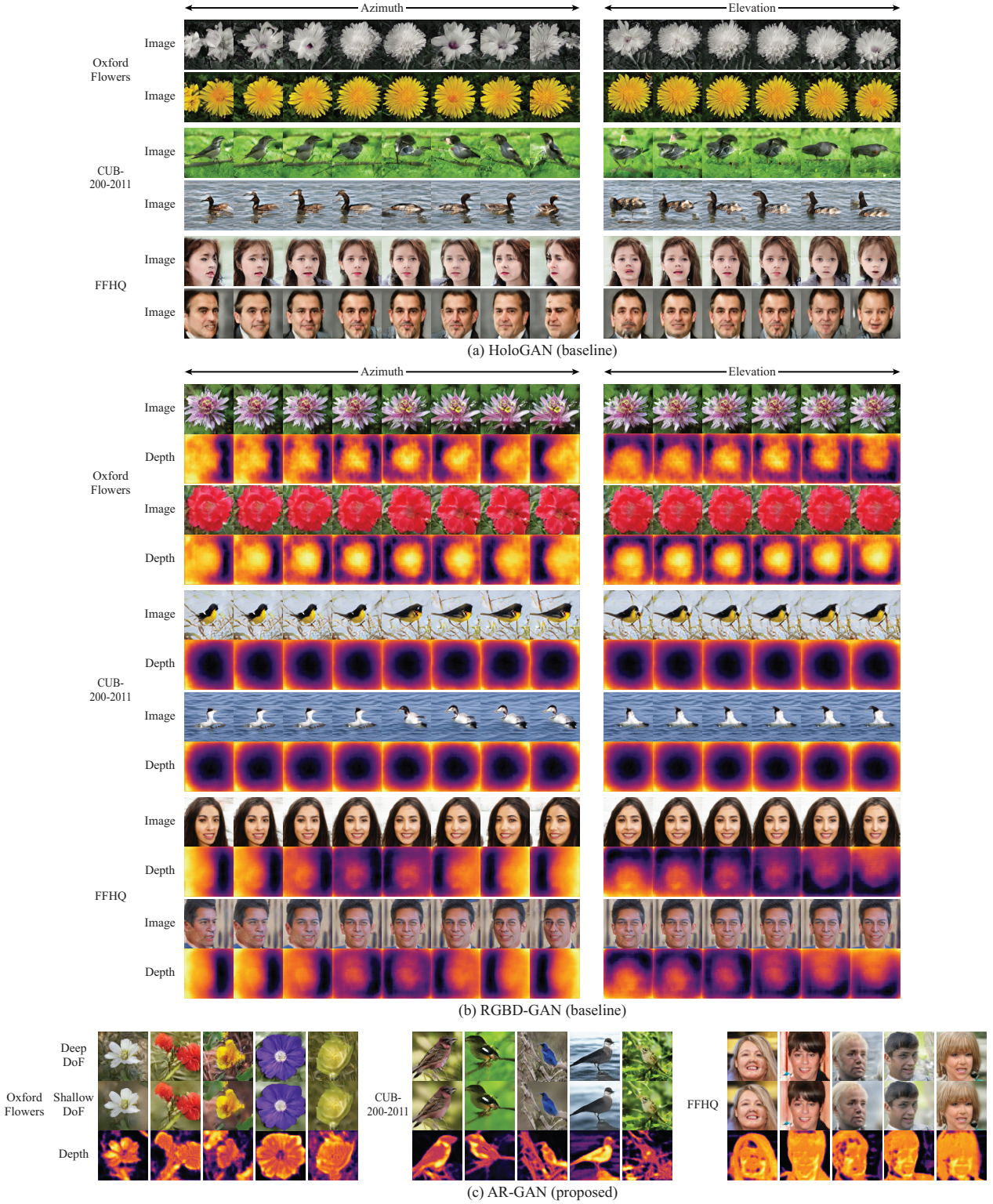


Figure 15. **Qualitative comparison among HoloGAN, RGBD-GAN, and AR-GAN.** This is an extended version of Figure 5. HoloGAN generates images only, RGBD-GAN generates image and depth pairs, and AR-GAN generates tuples of deep and shallow DoF images and depths. The respective sets are shown in the same column in each image block. When viewpoint distributions are biased (i.e., Oxford Flowers and CUB-200-2011), HoloGAN and RGBD-GAN have difficulty in learning 3D representations (e.g., in (a), the bird direction does not change smoothly in HoloGAN on CUB-200-2011), whereas AR-GAN succeeds in learning the depth and DoF effect in all datasets.

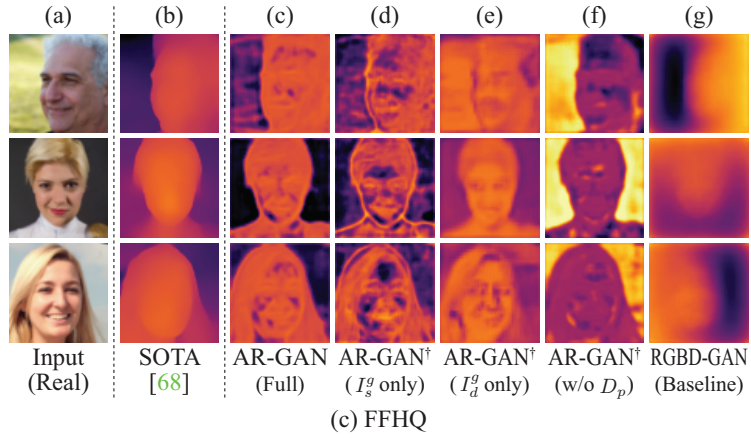
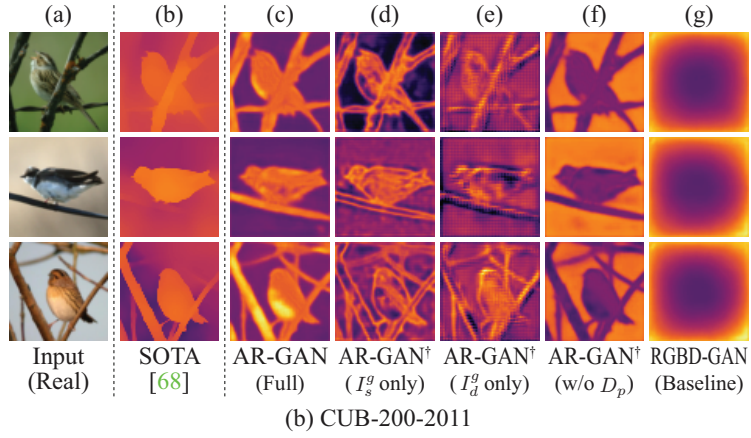
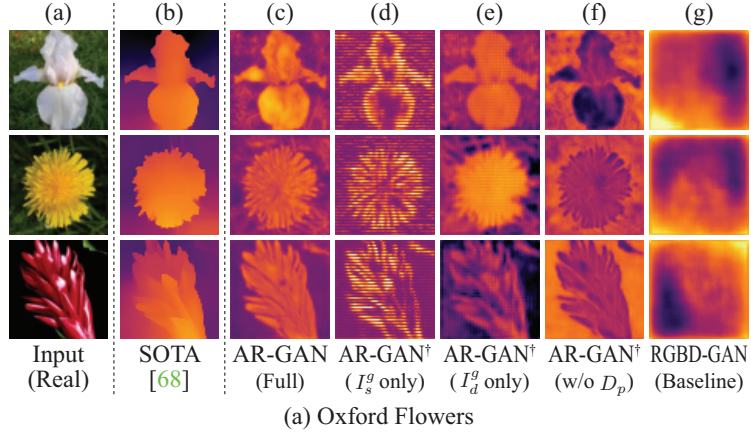


Figure 16. **Examples of predicted depths.** This is an extended version of Figure 6. (b) Results obtained using a state-of-the-art (SOTA) monocular depth estimator [68], which was trained using stereo pairs in an external dataset. (c–g) Results obtained in a fully unsupervised setting. Particularly in (c), AR-GAN with DoF mixture learning and center focus prior was used. In (d–f), [†] indicates the ablated model, and either DoF mixture learning or the center focus prior was ablated. In (g), RGBD-GAN was used.

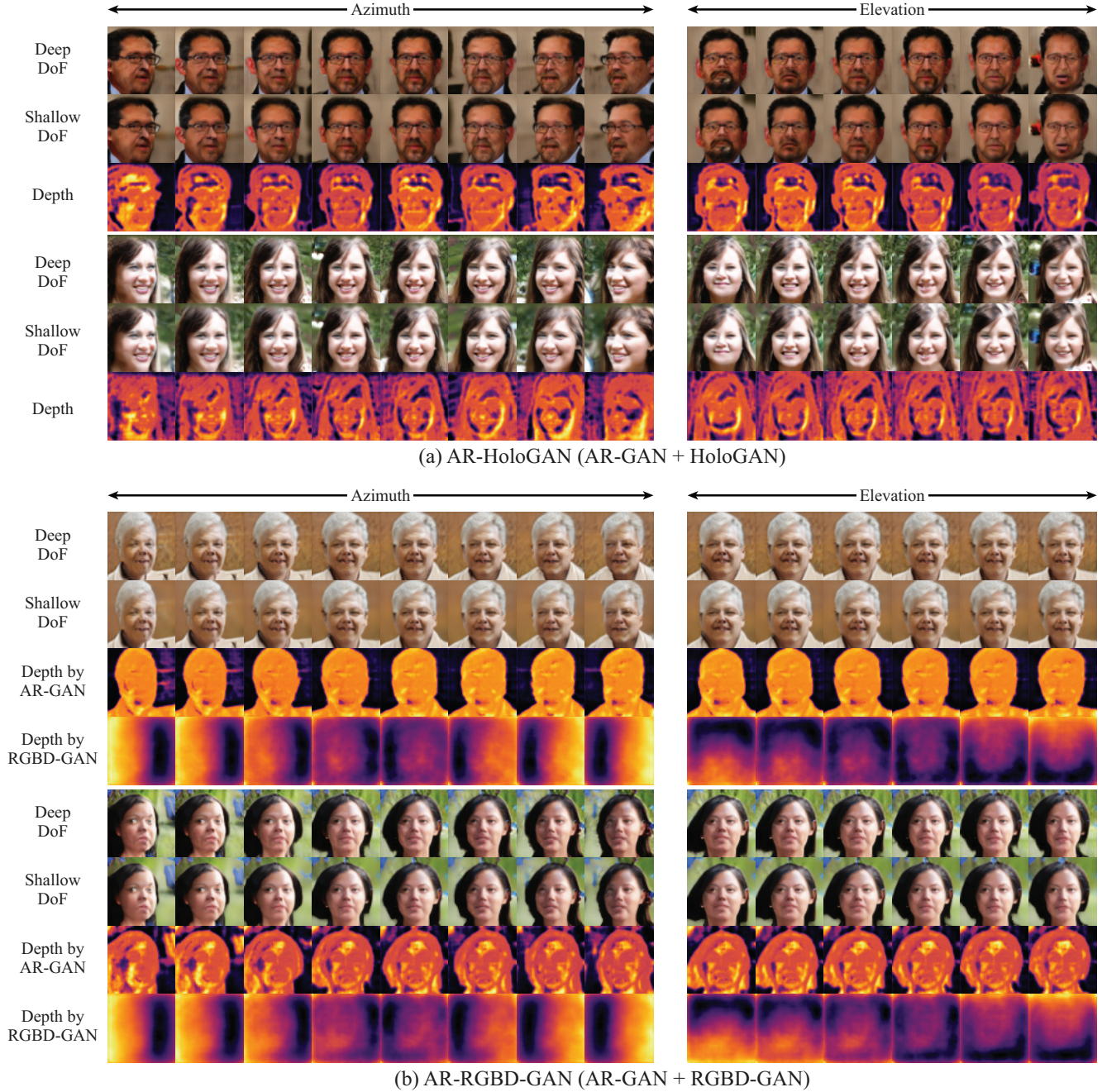


Figure 17. **Examples of data generated using AR-HoloGAN and AR-RGBD-GAN.** This is an extended version of Figure 8. The viewpoint change in the horizontal direction is obtained by the HoloGAN/RGBD-GAN function, whereas the DoF change and depth in the vertical direction (in the top three rows in each image block) are obtained by the AR-GAN function. With regard to AR-RGBD-GAN, we also visualized the depth predicted by the RGBD-GAN function in the bottom row. Two types of depths (i.e., the depth predicted by AR-GAN and the depth predicted by RGBD-GAN) do not completely match because they are calculated based on different principles. The depth predicted by AR-GAN is based on *focus cues*, whereas the depth predicted by RGBD-GAN is based on the *consistency between viewpoints*.



Figure 18. **Examples of shallow DoF rendering.** This is an extended version of Figure 9. CycleGAN often yields unnecessary changes (e.g., color change in the first row or overblurring of the main object (i.e., the flower) in the eighth row), whereas AR-GAN-R and AR-GAN-DR do not. The generated shallow DoF images were almost the same for AR-GAN-R and AR-GAN-DR. The main difference between them is that AR-GAN-DR can estimate the depth simultaneously, whereas AR-GAN-R cannot.

C. Implementation details

In this appendix, we provide implementation details for the following items:

- Appendix C.1: Implementation details of 64×64 image generation, which were used in the experiments in Sections 5.2–5.4.
- Appendix C.2: Implementation details of 128×128 image generation, which were used to generate samples in Figure 1.
- Appendix C.3: Implementation details of shallow DoF rendering, which were used in the experiments in Section 5.5.

Notation. In our description of the network architectures, we use the following notation.

- Linear: Linear layer
- Conv: Convolutional layer
- Deconv: Deconvolutional (i.e., fractionally strided convolutional) layer
- ReLU: Rectified linear unit [43]
- LReLU: Leaky rectified linear unit [41, 69]
- IN: Instance normalization [57]
- AdaIN: Adaptive instance normalization [20]
- SN: Spectral normalization [42]

In our description of the training settings, we use the following notation. We used the Adam optimizer [31] for training.

- α : Learning rate
- β_1 : First-order momentum parameter
- β_2 : Second-order momentum parameter

C.1. Details of image generation (Sections 5.2–5.4)

Network architectures. Table 9 provides the AR-GAN architecture for 64×64 images. This was used in the experiments in Sections 5.2–5.4. As mentioned in Section 5, we designed the generator (Table 9(a)) and discriminator (Table 9(c)) based on HoloGAN [44],¹² which was used as a baseline in the experiments. In HoloGAN, 3D transformation and 3D convolution were used in the generator. However, they are not required in AR-GANs. Therefore, in AR-GAN, we removed the 3D transformation and replaced the 3D convolution with a 2D convolution.

The generator (Table 9(a)) has a StyleGAN-like architecture [29], in which the latent vector z is inserted into the network using adaptive instance normalization (AdaIN(z)) [20]. In the last layer of the generator, we adjusted the scale of D in an instance-dependent manner using a constant (i.e., 10) and a one-hidden-layer multilayer perceptron (MLP(z)). Table 9(b) provides the architecture of

(a) Generators G_I and G_D	
Input 1: Constant $c \in \mathbb{R}^{4 \times 4 \times 1024}$, Input 2: Random noise $z \in \mathbb{R}^{128} \sim \mathcal{N}(0, 1)$	
c , AdaIN(z), ReLU	
4×4 Deconv up 512, AdaIN(z), ReLU	
4×4 Deconv up 256, AdaIN(z), ReLU	
4×4 Deconv up 128, AdaIN(z), ReLU	
4×4 Deconv up 64, AdaIN(z), ReLU	
4×4 Conv 3, Tanh $\rightarrow I_d^g$	
4×4 Conv 1, Tanh $\times 10 \times \text{MLP}(z) \rightarrow D^g$	
(b) Depth expansion network T	
Input: Warped depth map $D(\mathbf{x} + \mathbf{u}D(\mathbf{x})) \in \mathbb{R}^{64 \times 64 \times 25}$	
3×3 Conv 25, IN, LReLU	
3×3 Conv 25, IN, LReLU	
3×3 Conv 25, IN, LReLU, Add input $\rightarrow M(\mathbf{x}, \mathbf{u})$	
(c) Discriminator C	
Input: Image $I \in \mathbb{R}^{64 \times 64 \times 3}$	
5×5 Conv down 64, LReLU	
5×5 SN Conv down 128, IN, LReLU	
5×5 SN Conv down 256, IN, LReLU	
5×5 SN Conv down 512, IN, LReLU	
Linear	

Table 9. AR-GAN architecture for 64×64 images.

the depth expansion network T , which was used in the aperture renderer (Section 3.2). In the aperture renderer, we set the aperture size to 5×5 . This was implemented based on a previous study on aperture rendering [53]. In the discriminator (Table 9(c)), we used instance normalization (IN) [57] and spectral normalization (SN) [42], following the implementation of HoloGAN.¹²

We implemented HoloGAN (used in Section 5.2) using the same network architecture that was used in the original study [44].¹² In the generator, the first and second 2D deconvolutional layers in Table 9(a) were replaced with 3D deconvolutional layers. After this processing, 3D transformation was performed, and then 1×1 Conv and ReLU were applied to adjust the number of channels. Strictly, we modified the number of channels following the official code.¹² In addition, we removed a depth estimation layer (which is presented at the bottom of Table 9(a)) because HoloGAN cannot optimize it. In HoloGAN, we used the same discriminator as the one used in AR-GAN (Table 9(c)).

We implemented the generator and discriminator in RGBD-GAN (used in Section 5.2) using almost the same network architecture as that of AR-GAN (Table 9). An exception is that we conducted a modification to the generator (Table 9(a)) to incorporate the viewpoint information (i.e., azimuth θ_a and elevation θ_e) into the network. More concretely, we concatenated $c_{cyclic} =$

¹²<https://github.com/thunguyenphuoc/HoloGAN>

$[\cos(\theta_a), \sin(\theta_a), \cos(\theta_e), \sin(\theta_e)]$ to z and used the combination of z and c_{cyclic} as the input of AdaIN in the first and second layers. In the initial experiments, we found that replacing the constant input c with c_{cyclic} (by converting c_{cyclic} using a CNN to match the size) is useful for learning the disentangled representations. Therefore, we applied this modification in the experiments. In addition, we modified the depth estimation layer at the bottom of Table 9(a) as “ 4×4 Conv 1, Tanh, Shift 1” because we found that this setting works reasonably well. In RGBD-GAN, we used the same discriminator as that used in AR-GAN (Table 9(c)).

When implementing AR-HoloGAN/AR-RGBD-GAN (used in Section 5.4), we added a depth estimation layer (shown at the bottom of Table 9(a)) to the last layer of the HoloGAN/RGBD-GAN generator. Through this modification, we generated I_d^g and D^g simultaneously, and then rendered the shallow DoF image (i.e., I_s^g) from (I_d^g, D^g) using the aperture renderer, similar to AR-GAN. In addition, in AR-HoloGAN and AR-RGBD-GAN, we used the same discriminator as that used in AR-GAN (Table 9(c)).

Training settings. As a GAN objective function, we used a non-saturating GAN loss [15]. We set the hyperparameters of the center focus prior (Equation 7) as $r_{th} = 0.25$ and $g = 1$, where we scale r (the distance from the center of the image) such that $r = 1$ represents half of the image width or height. We set the weighting parameter λ_p (Equation 8) to 1. We used the center focus prior only during the initial $5k$, $5k$, and $50k$ iterations on Oxford Flowers, CUB-200-2011, and FFHQ, respectively. Following a previous study [53], we regularized the depth expansion network T so that the predicted depth map $M(\mathbf{x}, \mathbf{u})$ was close to the warped versions of $D(\mathbf{x})$:

$$\mathcal{L}_d = \lambda_d \|M(\mathbf{x}, \mathbf{u}) - D(\mathbf{x} + \mathbf{u}D(\mathbf{x}))\|_1, \quad (9)$$

where λ_d is the weighting parameter and set to 1 in the experiments.

We trained the networks from scratch using the Adam optimizer [31] with $\alpha = 0.0001$, $\beta_1 = 0.5$, $\beta_2 = 0.999$, and a batch size of 32. Following the implementation of HoloGAN, we updated the generator twice for every update of the discriminator. We updated the discriminator for $150k$, $250k$, and $350k$ iterations on Oxford Flowers, CUB-200-2011, and FFHQ, respectively. To stabilize the training, we applied differentiable augmentation [74], including color jittering, translation, and cutout [7]. To obtain a stable performance, we used an exponential moving average [28] with a decay of 0.999 over the weights to produce the final generator.

When training HoloGAN, RGBD-GAN, AR-HoloGAN, and AR-RGBD-GAN, we sampled the azimuth and elevation uniformly within the range of $[-50, 50]$ and $[-20, 20]$, respectively, because such range values were used as default values in HoloGAN and RGBD-GAN (particularly, on a face image dataset).

(a) Generators G_I and G_D	
Input 1: Constant $c \in \mathbb{R}^{4 \times 4 \times 1024}$, Input 2: Random noise $z \in \mathbb{R}^{128} \sim \mathcal{N}(0, 1)$	
c , AdaIN(z), ReLU	
4×4 Deconv up 1024, AdaIN(z), ReLU	
4×4 Deconv up 512, AdaIN(z), ReLU	
4×4 Deconv up 256, AdaIN(z), ReLU	
4×4 Deconv up 128, AdaIN(z), ReLU	
4×4 Deconv up 64, AdaIN(z), ReLU	
4×4 Conv 3, Tanh $\rightarrow I_d^g$ 4×4 Conv 1, Tanh $\times 10 \times \text{MLP}(z) \rightarrow D^g$	
(b) Depth expansion network T	
Input: Warped depth map $D(\mathbf{x} + \mathbf{u}D(\mathbf{x})) \in \mathbb{R}^{128 \times 128 \times 25}$	
3×3 Conv 25, IN, LReLU	
3×3 Conv 25, IN, LReLU	
3×3 Conv 25, IN, LReLU, Add input $\rightarrow M(\mathbf{x}, \mathbf{u})$	
(c) Discriminator C	
Input: Image $I \in \mathbb{R}^{128 \times 128 \times 3}$	
5×5 Conv down 64, LReLU	
5×5 SN Conv down 128, IN, LReLU	
5×5 SN Conv down 256, IN, LReLU	
5×5 SN Conv down 512, IN, LReLU	
Linear	

Table 10. AR-GAN architecture for 128×128 images.

C.2. Details of image generation (Figure 1)

Network architectures. Table 10 provides the AR-GAN architecture for 128×128 images. This was used for generating samples in Figure 1. This network architecture is similar to that for 64×64 images (Table 9) except that one layer is added to the generator according to the change in image size.

Training settings. We used similar training settings as those for 64×64 images (Section C.1) except that the hyperparameters of the center focus prior were modified as $r_{th} = 0.25$ and $g = 2$ according to the change in image size. We used the center focus prior only during the initial $5k$, $5k$, and $5k$ iterations on Oxford Flowers, CUB-200-2011, and FFHQ, respectively.

C.3. Details of shallow DoF rendering (Section 5.5)

Network architectures. Table 11 provides the AR-GAN-DR depth estimator architecture. We used the u-net architecture [49]. The AR-GAN-R image translator has a similar architecture to this, except that the number of channels of the last layer is modified to three to generate an RGB image. These models were used in the experiments in Section 5.5.

Training settings. We generated training data (i.e., pairs of images and depths) using the AR-GAN that was trained

Input: $I_d \in \mathbb{R}^{128 \times 128 \times 3}$	
ENC_CONV0	3×3 Conv 48, LReLU
ENC_CONV1	3×3 Conv 48, LReLU
POOL1	2×2 Maxpool
ENC_CONV2	3×3 Conv 48, LReLU
POOL2	2×2 Maxpool
ENC_CONV3	3×3 Conv 48, LReLU
POOL3	2×2 Maxpool
ENC_CONV4	3×3 Conv 48, LReLU
POOL4	2×2 Maxpool
ENC_CONV5	3×3 Conv 48, LReLU
POOL5	2×2 Maxpool
ENC_CONV6	3×3 Conv 48, LReLU
UPSAMPLE5	2×2 Upsample
CONCAT5	Concatenate output of POOL4
DEC_CONV5A	3×3 Conv 96, LReLU
DEC_CONV5B	3×3 Conv 96, LReLU
UPSAMPLE4	2×2 Upsample
CONCAT4	Concatenate output of POOL3
DEC_CONV4A	3×3 Conv 96, LReLU
DEC_CONV4B	3×3 Conv 96, LReLU
UPSAMPLE3	2×2 Upsample
CONCAT3	Concatenate output of POOL2
DEC_CONV3A	3×3 Conv 96, LReLU
DEC_CONV3B	3×3 Conv 96, LReLU
UPSAMPLE2	2×2 Upsample
CONCAT2	Concatenate output of POOL1
DEC_CONV2A	3×3 Conv 96, LReLU
DEC_CONV2B	3×3 Conv 96, LReLU
UPSAMPLE1	2×2 Upsample
CONCAT1	Concatenate output of INPUT
DEC_CONV1A	3×3 Conv 64, LReLU
DEC_CONV1B	3×3 Conv 32, LReLU
DEC_CONV1C	3×3 Conv 1 $\rightarrow D$

Table 11. **AR-GAN-DR depth estimator architecture.**

using 128×128 images on Oxford Flowers. This AR-GAN was the same as that used for generating the samples in Figure 1. We trained the depth estimator for $300k$ iterations using the Adam optimizer [31] with $\alpha = 0.0003$, $\beta_1 = 0.9$, $\beta_2 = 0.99$, and a batch size of 4. The learning rate was kept constant during the training, except for the last 30% iterations, where the learning rate was smoothly ramped down to zero.